Cortex-Wide, Cellular-Resolution Volumetric Imaging with a Modular Two-Photon Imaging Platform

Jiahao Hu[1#], Yanfeng Zhu[1#], Shoupei Liu[1#], Chengyu Li[1], Min Zhang[1], Xinyang Gu[2], Jingchuan Wu[2], Fang Xu[3], Liang Chen[2], Ying Mao[2], Bo Li[1,2*]

[1]Huashan Hospital, MOE Frontiers Center for Brain Science, State Key Laboratory of Brain Function and Disorders, Institutes for Translational Brain Research, Jinshan Hospital, Fudan University, Shanghai 200032, China

[2]Department of Neurosurgery, Huashan Hospital, Shanghai Medical College, Fudan University, Shanghai 200040, China.

[3]Interdisciplinary Center for Brain Information, Brain Cognition and Brain Disease Institute, Shenzhen Institutes of Advanced Technology, Chinese Academy of Sciences; Shenzhen, 518055, China.

*Correspondence: liboresearch@gmail.com (B. L.)

Abstract

Mapping cortex-wide neuronal activity at single-cell resolution has been limited by the physical trade-off between numerical aperture and field-of-view (FOV) in two-photon microscopes. We present Meso2P, a modular two-photon platform that decouples excitation and detection by introducing a lateral paraboloid fluorescence collector. The design sustains an effective NA 0.87 over a contiguous 6 × 6 mm^2 FOV at high speed (2,048 × 2,048 pixels at 7.67 Hz). The modular platform can be upgraded with optional modules for simultaneous multi-plane imaging (1-4 planes at full resolution and speed), volumetric imaging (6 × 6 × 0.5 mm^3, 2,048 × 2,048 × 28 voxels at 1 Hz capturing > 210,000 neurons), and holographic two-photon optogenetic stimulation for targeted perturbations. To handle the resulting large-scale data, we provide an open-source deep-learning pipeline that automates motion correction, segmentation, and spike inference. We demonstrate cortex-wide sensory responses, layer-specific network synchrony during anaesthesia, and in-vivo tracking of micro- and nanoplastic distribution. Meso2P therefore provides a reproducible route to high-throughput volumetric imaging across almost the entire cortex with high detection efficiency.

31 # Introduction

32 Understanding how spatially distributed cortical circuits cooperate to generate
33 perception and behaviour[1-3] requires imaging tools that record activity from multiple
34 brain regions simultaneously and with single-cell resolution[4]. Two-photon (2P)
35 microscopy offers intrinsic optical sectioning, micron-scale resolution and
36 compatibility with genetically encoded indicators, and has therefore become the
37 work-horse of cellular neurophysiology[5-12]. Yet conventional designs image less than
38 1 mm^2 per frame, obliging researchers to trade breadth for detail and to rely on
39 sequential recordings when probing cortex-wide dynamics[13].

40 Large-field-of-view (FOV) mesoscopes have begun to relax this constraint by
41 scaling scan angles and using custom objectives with entrance pupils exceeding 25
42 mm. These instruments can span several millimetres, but the required long focal
43 lengths inevitably lower their numerical aperture (NA ≈ 0.4-0.5)[13-21], reducing
44 fluorescence collection efficiency, compromising deep-tissue sensitivity[22] and
45 introducing field curvature[23]. Add-on volumetric modules—Bessel beams[24], spatial
46 multiplexing[25], or light-field optics[17]—restore 3D coverage but inherit the parent
47 system's limited NA and are often incompatible with 2P optogenetic stimulation. In
48 parallel, the massive data streams (> 100 GB h^{-1}) produced by centimetre-scale
49 imaging strain existing analysis pipelines, which were designed for thousands rather
50 than hundreds of thousands of neurons[17, 26-28].

51 At the heart of these challenges lies a simple physical coupling: for a single
52 objective with shared excitation and detection paths, NA × FOV is approximately
53 proportional to the objective diameter ($D \approx 2 \times f \times NA$). As FOV grows, maintaining
54 high NA demands impractically large optics and scan apertures. Because fluorescence
55 signal in scattering tissue scales with the square of NA, any drop in collection
56 efficiency disproportionately penalises volumetric imaging, where excitation power
57 must already be divided across multiple planes. Breaking the NA-FOV coupling is
58 therefore essential for a practical, cortex-wide cellular imager.

59 Here, we introduce Meso2P, a modular 2P platform that eliminates this trade-off

by physically separating excitation and detection. Its key advances are: first, a paraboloid lateral collection module decouples detection from excitation, preserving an effective NA 0.87 and uniform diffraction-limited resolution across a 6 × 6 mm^2 cortical window at high speed (2048 × 2048 pixels at 7.67 Hz); second, a modular imaging architecture supports simultaneous multi-plane imaging (1-4 planes at full resolution and speed), volumetric imaging (6 × 6 × 0.5 mm^3, 2048 × 2048 × 28 voxels at 1 Hz), and two-photon optogenetic stimulation; third, an open-source deep-learning pipeline (NeuroPixelAI) motion-corrects, segments and deconvolves calcium signals from > 200,000 neurons in 100 GB datasets on a standard workstation.

Results

Implementation of Meso2P for High-Efficiency, Mesoscale Two-Photon Imaging

Meso2P integrates four plug-and-play modules for a centimetre-scale, cellular-resolution imaging and perturbation platform (Fig. 1): (1) a custom wide-angle scan relay for micron-resolution imaging across a 6 × 6 mm^2 FOV; (2) a lateral paraboloid fluorescence collection module that decouples detection from excitation and raises the effective NA to 0.87; (3) a multiplexing module that enables simultaneous multi-plane imaging, which can be further upgraded to volumetric imaging by adding a piezo-driven axial scanning stage; (4) a two-photon optogenetics module for cellular-resolution perturbation.

The custom scan relay delivers diffraction-limited, uniform imaging over centimetre-scale fields. Galvo-resonant mirrors scanning through ± 13° are relayed by a custom-designed optics chain comprising several scan lenses, a tube lens, an aberration compensation module, and a 4× objective (Fig. 1A, Extended Data Fig. 1B). Wavefront errors remain < 0.1 λ RMS throughout the scan range, with uniform image brightness preserving subcellular fidelity across the entire FOV (Extended Data Fig. 1C,D). Unlike widely used mesoscopes that exhibit pronounced field curvature (~ 66.7 μm/mm)[23], Meso2P maintains negligible curvature (~ 5.57 μm/mm) as validated by uniform fluorescence from thin ruler imaging (Extended Data Fig. 1E). The resulting configuration achieves diffraction-limited lateral and axial resolutions of 0.6

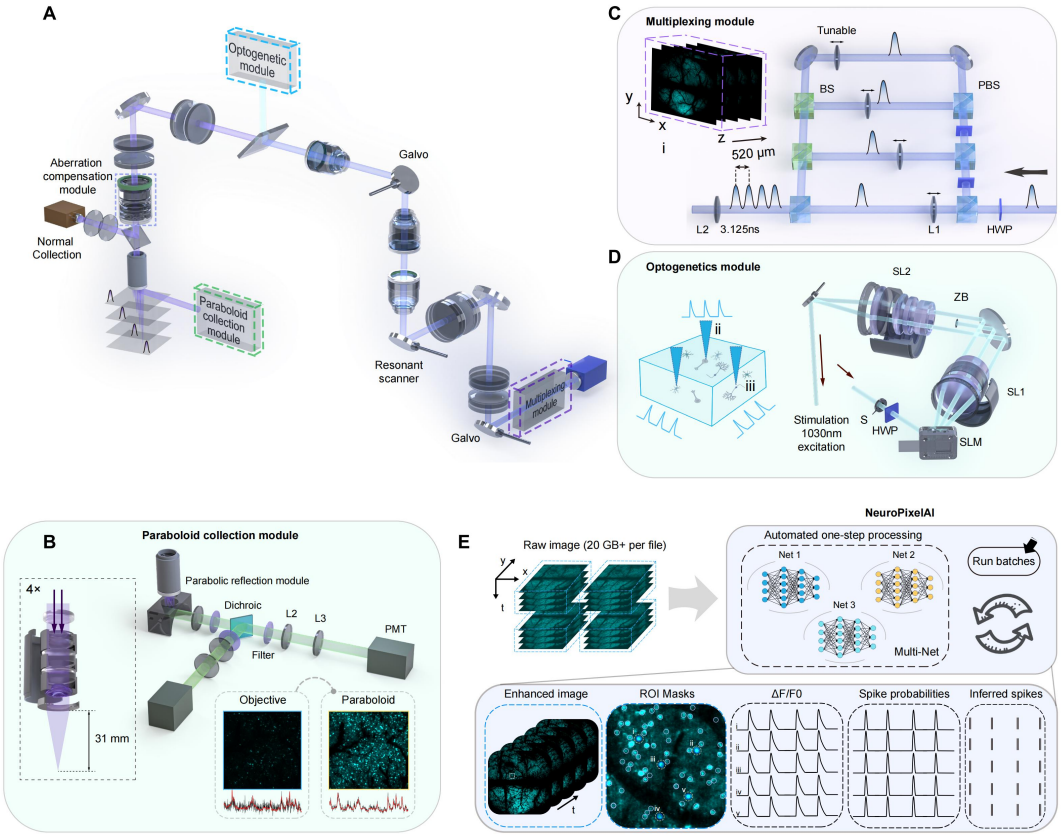

Fig. 1 Schematic overview of the Meso2P system. (A) Optical schematic of Meso2P. **(B)** Working principle of the lateral paraboloid collection module. **(C)** Multi-plane free imaging enabled by a time-division multiplexing module combined with piezoelectric z-scanning. **(D)** Optical layout of the SLM-based two-photon holographic stimulation module. S, shutter; HWP, half-wave plate; SL1-2, scan lenses; SLM, spatial light modulator; ZB, zero order block. **(E)** NeuroPixelAI, an integrated deep learning-based analysis pipeline for high-throughput segmentation and calcium signal extraction from mesoscale two-photon datasets. ***See also* Extended Data Fig. 1,2 and Video S1**.

μm and 11.7 μm, respectively, across a 6 × 6 mm² FOV (Extended Data Fig. 1F). Alternative objectives, such as a commercial 16×, can be integrated to flexibly trade spatial resolution for imaging area (Extended Data Fig. 1G).

Decoupling fluorescence detection from excitation breaks the NA-FOV coupling, significantly enhancing photon collection. Conventional large-FOV two-photon systems enlarge objective diameters to increase NA, yet remain fundamentally constrained by the NA × FOV relationship ($D \approx 2 \times f \times NA$). Meso2P circumvents this limit by introducing an aluminium-coated paraboloid fluorescence collection module positioned laterally between the objective and sample (Fig. 1B, Extended Data Fig. 1H). Excitation via the 4× objective at NA 0.30 provides adequate

108 micron-level resolution for large-scale imaging, while fluorescence collection benefits
109 from an effective NA of 0.87 across a 6 × 6 mm^2 area, outperforming conventional
110 and custom large-diameter objectives (Extended Data Fig. 1A). Uniformity in
111 point-spread-function peak intensity and collection efficiency (< 10% variation)
112 ensures consistent high-quality imaging without oversized optics (Extended Data Fig.
113 1I). A quantitative side-by-side benchmarking against representative large-FOV
114 two-photon platforms is provided in Supplementary Note 1 and Table 1-3.

115 The multiplexing module enables safe, high-throughput and simultaneous
116 multi-plane imaging. Each laser pulse is divided into four temporally separated
117 sub-pulses (~ 3.125 ns apart), simultaneously exciting multiple focal planes separated
118 by ~ 130 μm, adjustable to cortical layers of interest (Fig. 1C, Extended Data Fig.
119 2A,B). Crucially, the inter-plane spacing is adjustable, allowing precise targeting of
120 anatomically defined cortical layers—such as layers 2/3 and 5 (Fig. 5)—and enabling
121 concurrent imaging of functionally distinct networks at different depths. This flexible
122 multi-plane capability is particularly valuable for studies requiring high-resolution,
123 cross-laminar interrogation of distributed brain regions, a configuration that has
124 remained unattainable with previous large-FOV systems (Table 1). Furthermore, the
125 system can be upgraded to volumetric imaging by combining four-plane multiplexing
126 with piezo-driven axial scanning. Piezo-driven axial scanning further divides each
127 plane into seven axial steps (18 μm spacing), creating a 6 × 6 × 0.5 mm^3 volume (3 ×
128 3 × 18 μm^3 voxel size) imaged at 1 Hz. Efficient single-point excitation combined
129 with high-NA detection enables robust imaging at a total laser power of ~ 250
130 mW—substantially lower than previous systems[25] and below the threshold for
131 heat-induced tissue damage, as confirmed by immunolabelling assays (Extended Data
132 Fig. 2C-F). Two-plane multiplexed imaging exhibits negligible crosstalk from
133 fluorescence lifetime overlap, while minor crosstalk in the four-plane mode is
134 effectively mitigated through a demixing process followed by analysis with the
135 NeuroPixelAI pipeline (Extended Data Fig. 2G).

136 Integrated two-photon optogenetic module ensures precise perturbation
137 capability. A spatial-light modulator generates user-defined holographic stimulation

138 patterns, dynamically scanned by galvanometric mirrors in spiral trajectories (Fig. 1D,
139 Extended Data Fig. 1B). Imaging and stimulation beams are seamlessly co-registered
140 via a dichroic mirror, achieving sub-micron spatial accuracy without additional
141 alignment steps.

142 NeuroPixelAI provides automated, scalable processing of large-scale calcium
143 imaging datasets. To efficiently handle extensive neuronal recordings—typically
144 containing tens of thousands of neurons across hundreds of thousands of frames—we
145 developed NeuroPixelAI, a dedicated computational pipeline leveraging deep learning
146 (Fig. 1E). The pipeline automates motion correction, image denoising, neuron
147 segmentation, calcium trace extraction, and spike inference, delivering rapid, robust,
148 and fully automated analysis with minimal user intervention.

149 **Characterization of Meso2P for high-speed, high-resolution mesoscale imaging**

150 Using Camk2α-GCaMP6s mice, we first assessed single-plane performance. At
151 7.67 Hz and 2,048 × 2,048 pixels/frame, the system resolved individual layer 2/3
152 neurons 250 μm below the dura across the entire 6 × 6 mm^2 FOV (Fig. 2A).
153 high-resolution mode (4,096 × 4,096 pixels, 3.83 Hz) is available when finer
154 morphology is required. Fluorescence intensity and point-spread function were
155 spatially uniform, enabling automated extraction of 13,586 neurons from 2000 frames
156 in a representative animal (Fig. 2B,C).

157 Side-collection proved essential for this throughput. Under identical excitation
158 power, the paraboloid mirror increased photon yield from ~ 4% (standard
159 epi-detection) to 53%, equivalent to NA 0.87 (Fig. 2D-F). This translated directly into
160 a ~ 10 dB increase in signal-to-background ratio and a 2.5-fold improvement in
161 neuron segmentation yield (Fig. 2G-I, Extended Data Fig. 3A), demonstrating that
162 decoupled detection directly enhances population imaging fidelity.

163 We next assessed volumetric performance. By capturing 28 axial planes across a
164 0.5 mm depth at 1 Hz, the system achieved high-speed, large-scale volumetric
165 recording (Fig. 2J, Extended Data Fig. 3B). In awake mice, this configuration
166 captured approximately 211,000 neurons spanning over 13 cortical areas (Fig. 2K,
167 Extended Data Fig. 3C)—an order-of-magnitude improvement compared to

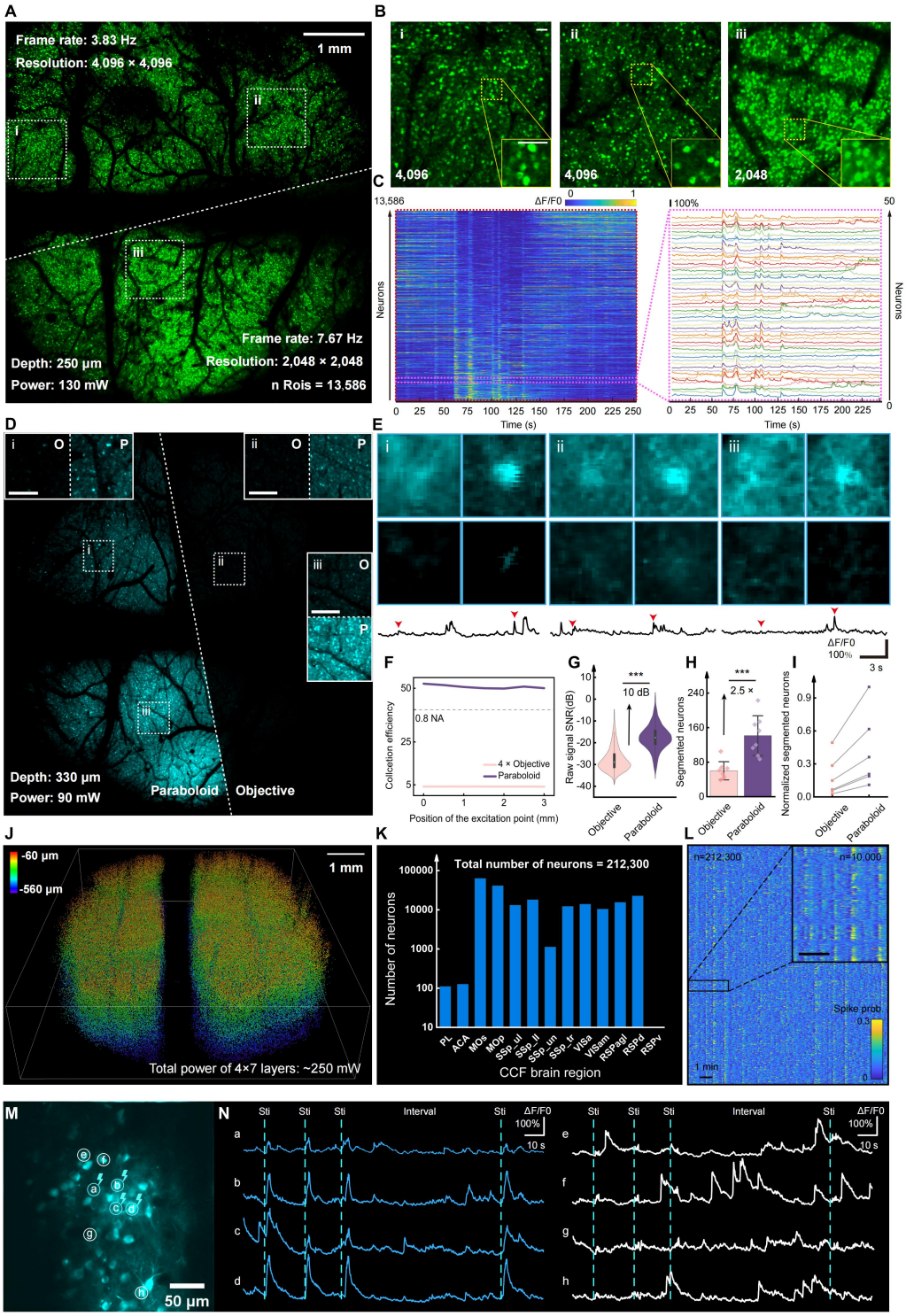

Fig. 2 Experimental characterizations and benchmarking of Meso2P. (A) *In vivo* calcium imaging of a transgenic mouse expressing GCaMP6s in excitatory neurons using Meso2P. Top, high-resolution mode (4,096 × 4,096 pixels, 3.83 Hz); Bottom, high-speed mode (2,048 × 2,048 pixels, 7.67 Hz). A total of 13,586 neurons were detected. **(B)** Zoom-in views of the regions marked in (A). **(C)** Heatmaps of calcium activity traces from neurons shown in (A); the zoom-in panel shows traces from 50 example neurons. **(D)** Comparison of image quality between fluorescence signals collected via the parabolic module (left) and direct detection through the objective (right). Three zoom-in views are included. **(E)** Representative neurons and calcium

traces obtained using the parabolic module (top) versus the objective (bottom). The red arrow indicates the recording time of the frames. **(F)** Comparisons of simulated collection efficiency obtained by the parabolic module (purple) and objective (pink). **(G)** Violin plot of the signal-to-noise ratios (SNR) from 10,466 neurons imaged with and without the parabolic module. ***$p < 0.001$; Tukey test. **(H)** Quantification of segmented neurons from eight randomly selected 700 µm × 700 µm regions in (D). Data presented as mean ± SD. Significance assessed by Tukey test: *$p < 0.05$, **$p < 0.01$, ***$p < 0.001$; n.s., not significant. **(I)** Normalized number of segmented neurons across various segmentation parameters for data with and without parabolic module. **(J)** 3D rendering of 10-minute recording from Meso2P. Neurons are color-coded by depth. **(K)** Histogram of neuron counts extracted across 12 cortical regions. **(L)** Heatmaps of spike probabilities from 212,300 neurons in (J). Zoom-in panel shows spike probabilities of 10,000 neurons. **(M)** Proof-of-concept two-photon photostimulation in layer 2/3 of the retrosplenial cortex. Four neurons (white circles) were simultaneously targeted for stimulation. **(N)** Left, calcium transients from the four photostimulated neurons showing the responses on all individual trials. Right, simultaneously recorded activity of four non-stimulated neurons. ***See also*** **Extended Data Fig. 3, Supplementary Video S2**.

one-photon light-field methods imaging similar volumes[17]. Calcium traces maintainedhigh signal-to-noise ratios throughout the volume (Fig. 2L).

Finally, we verified optogenetic compatibility. Fluorescent test slides confirmed the galvo/SLM path accurately generated arbitrary holographic patterns (Extended Data Fig. 3D). *In vivo*, simultaneous two-photon stimulation of four C1V1-expressing neurons produced synchronous calcium transients restricted to targeted cells, with off-target neurons remaining inactive (Fig. 2M,N). This proof-of-concept demonstrates sub-cellular co-registration of imaging and perturbation channels within the same optical core.

NeuroPixelAI enables scalable and automated analysis of mesoscale calcium imaging

NeuroPixelAI is an open-source, GPU-accelerated pipeline that converts raw mesoscale imaging data into spike trains via automated motion registration, deep-learning denoising, region-adaptive segmentation, baseline-corrected trace extraction, and spike inference (Fig. 3A,B, Extended Data Fig. 4A). A streaming phase-correlation algorithm with dynamic memory allocation processes a 30-GB file in a single pass on a standard 128-GB workstation, while plug-in support for neural networks such as DeepCAD-RT[29] and SRDTrans[30] effectively suppresses shot noise

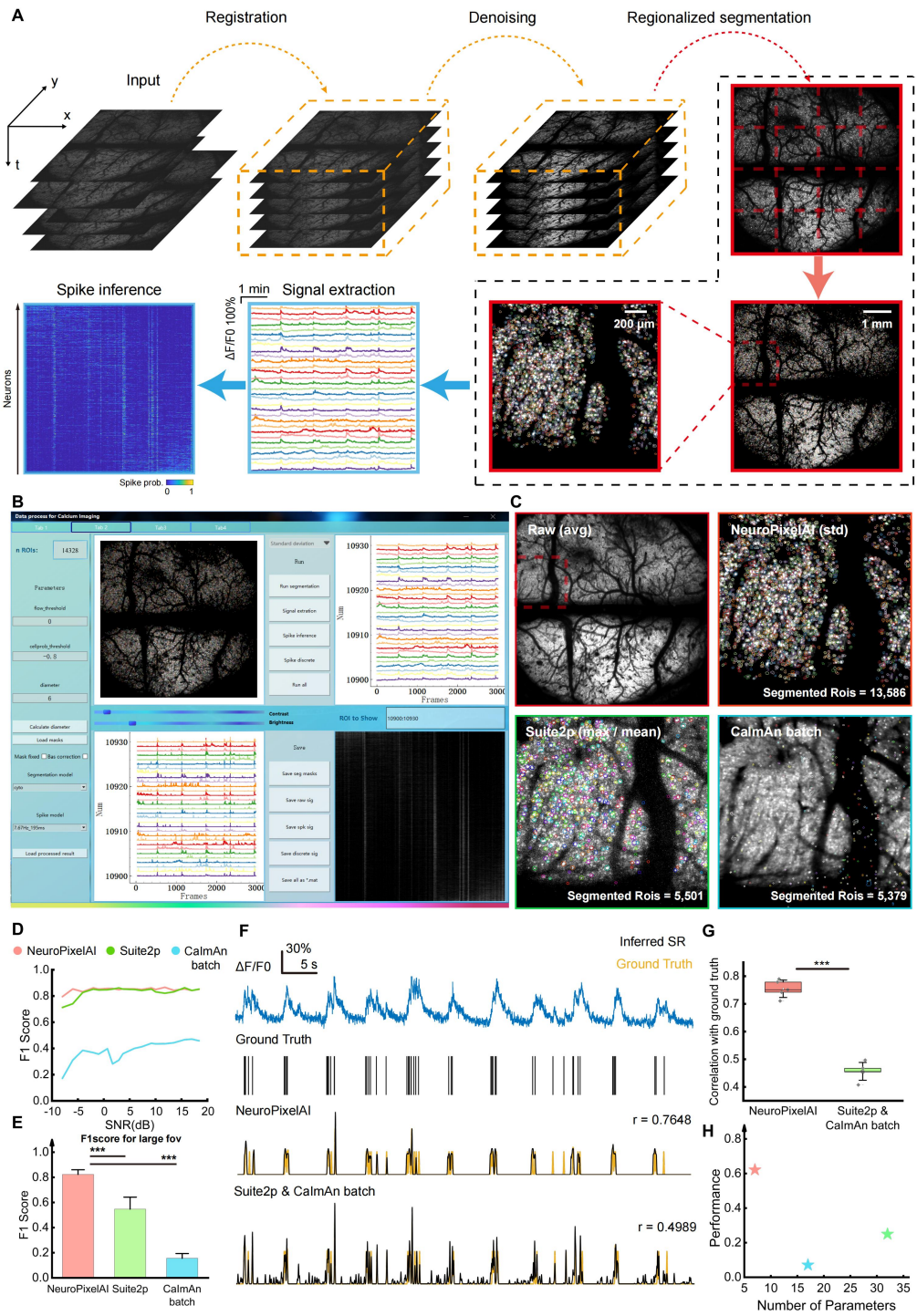

Fig. 3 Development and Benchmarking of NeuroPixelAI pipeline. (A) Schematic of the NeuroPixelAI processing pipeline, comprising five sequential modules: registration, denoising, regionalized segmentation, signal extraction, and spike inference. **(B)** Representative user interface of NeuroPixelAI. **(C)** Comparative segmentation results on a large FOV dataset. Top left, mean projection of raw fluorescence image. Top right, zoomed-in standard deviation projection with NeuroPixelAI segmentation. Bottom left, Suite2p segmentation (max / mean projection). Bottom right, CaImAn batch segmentation (mean projection). **(D)** F1 score comparison of neuron segmentation performance across the three pipelines on a simulated small FOV (300 μm × 300 μm) dataset generated by NAOMI with Gaussian-Poisson mixed noise. **(E)** F1 score comparison on a

221 large FOV dataset (6,000 μm × 6,000 μm). Ten subregions (1,500 μm × 1,500 μm) were randomly
222 sampled for evaluation. Mean ± SD; ***$p < 0.001$; Tukey test. **(F)** Comparisons of spike inference
223 outputs of NeuroPixelAI, Suite2p and CaImAn batch on the same dataset. **(G)** Correlations
224 between inferred spike trains and electrophysiological ground truth across NeuroPixelAI, Suite2p
225 and CaImAn batch. Mean ± SD; ***$p < 0.001$; Tukey test. **(H)** NeuroPixelAI achieves higher
226 overall performance (defined as average F1 score × correlation with ground truth) while
227 maintaining a compact set of seven parameters, only 2–4 of which typically require user
228 adjustment, outperforming other pipelines. ***See also*** **Extended Data Fig. 4, Supplementary**
229 **Video S3.**

230 and detector artefacts (Extended Data Fig. 4B,C). Segmentation leverages Cellpose
231 2.0 within a region-adaptive mask, ensuring reliable soma identification across
232 heterogeneous cortical areas (Extended Data Fig. 4D-F). Cubic-spline correction
233 (Extended Data Fig. 4G) removes baseline drift before Cascade-based spike inference
234 (Extended Data Fig. 4H-J). An iterative, label-free ranking module allows real-time
235 visualization of population activity (Extended Data Fig. 4K).

236 Compared to Suite2p and CaImAn[26, 27], NeuroPixelAI processes large files
237 directly without manual file splitting. It achieves substantial improvements in
238 segmentation accuracy (F1-score) on large-FOV data—by ~ 50% over Suite2p and ~
239 300% over CalmAn (Fig. 3C-E), and nearly doubles spike-inference fidelity on
240 GENIE datasets (Fig. 3F,G)[31, 32]. These advantages are achieved with only seven
241 adjustable parameters (typically 2-4 require minor adjustments per dataset), ensuring
242 a lightweight, robust workflow (Fig. 3H). Practically, a one-hour Meso2P dataset (>
243 200,000 neurons, > 100 GB) can be automatically processed into analysis-ready spike
244 trains within a few hours, transforming large-scale calcium imaging analysis from a
245 bottleneck into a routine laboratory task.

246 **Cortex-wide neuronal dynamics during whisker stimulation**

247 The mammalian neocortex integrates sensory information through distributed
248 cortical networks, establishing robust yet flexible regional co-fluctuation patterns
249 critical for perception[22, 33-37]. However, it remains poorly understood whether the
250 adaptive reorganization induced by repeated sensory stimuli propagates exclusively
251 within subnetworks or elicits global network-wide reorganization[36-39]. Conventional
252 wide-field approaches capture the spatial extent of such dynamics but are limited by

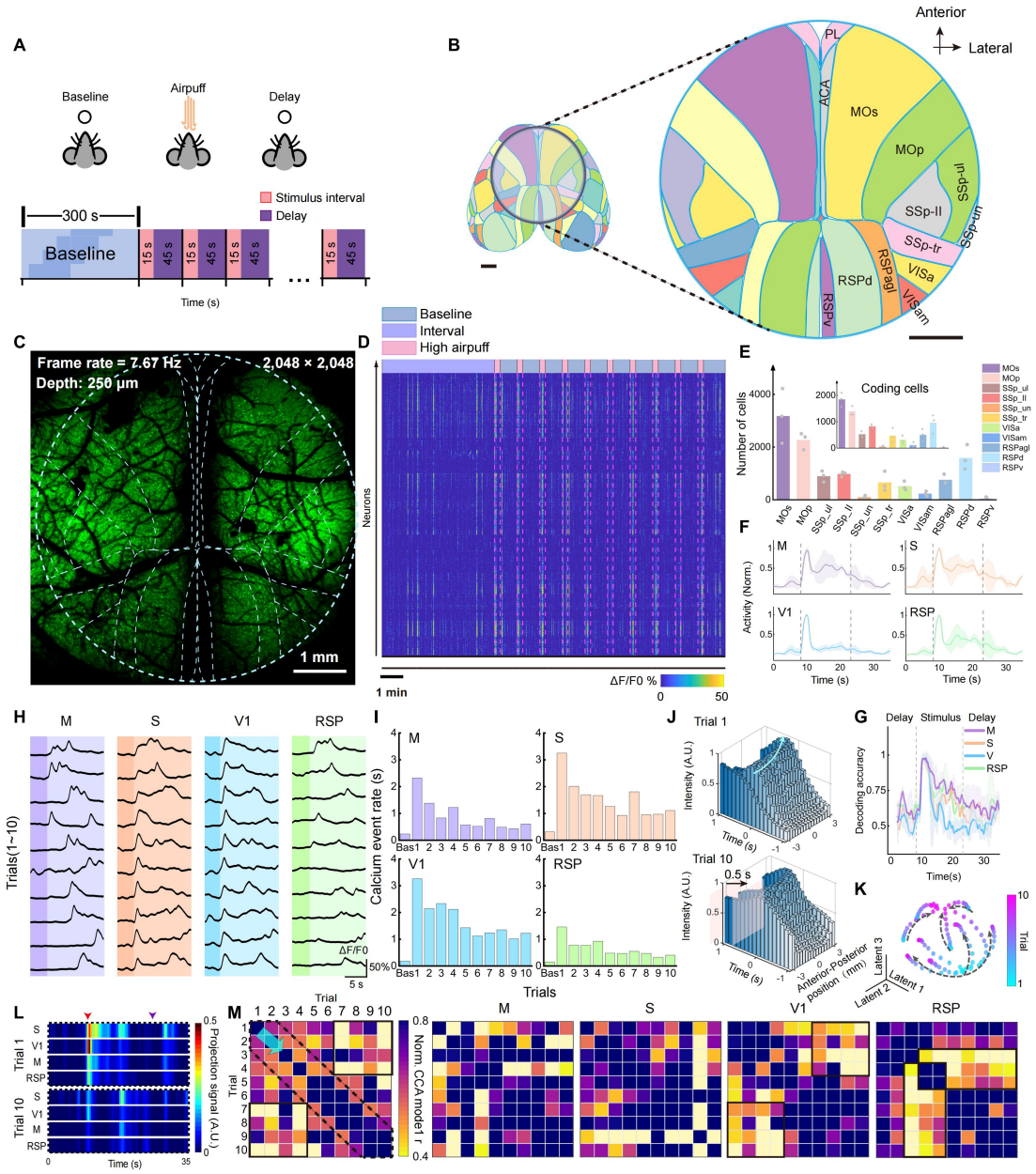

Fig. 4 Reorganization of whole-cortex population coding patterns during repetitive whisker stimulation. (A) Experimental schematic of the whisker stimulation paradigm. Each session began with a 300 s baseline, followed by ten trials of 15 s air-puff stimulus and 45 s inter-trial intervals. **(B)** Imaging field and anatomical landmarks. Scale bar, 1 mm. Inset: magnified cortical map. PL, prelimbic cortex; ACA, anterior cingulate area. M, motor cortex; S, somatosensory cortex; V1, primary visual cortex; RSP, retrosplenial cortex. The same abbreviations are used in all subsequent figures. **(C)** Standard deviation projection of the calcium imaging video showing > 10,000 neurons, overlaid with cortical area boundaries. **(D)** Heatmaps of calcium signals extracted from neurons in (C). Pink dashed lines indicate stimulus onset in each trial. **(E)** Mean numbers of neurons detected per brain region across mice (11,941 ± 3,193 neurons, mean ± SD; n = 3 mice). Gray dots represent individual animals. Inset: histogram of neurons active across all 10 trials. **(F)** Normalized activity of 4 cortical regions aligned to locomotion onset (vertical dashed line; n = 3 mice). Shaded area represents mean ± SD. **(G)** Mean classification accuracy of stimulus identity

267 across trials using SVM based on regional activity. Dashed lines denote stimulus onset and delay
268 time. Data are presented as mean ± SD (n = 3 mice). **(H)** Trial-by-trial calcium traces from
269 representative neurons across 4 cortical regions. Dark shading, delay period; Light shading,
270 stimulation period. **(I)** Bar plot of average calcium event rate of the 4 cortical regions over
271 baseline and 10 trials. **(J)** Top, bar plots of normalized neuron spike probability at each time point
272 and anterior-posterior bin in trial 1. The blue line indicates the direction of propagation of the
273 peak-signal arrival time. Bottom, same analysis in trial 10. The transparent pink walls mark the
274 peak-signal arrival time in trial 1 and trial 10, respectively. **(K)** 3D CEBRA-Time visualization
275 (on spike probabilities) of neural recording across ten trials in a representative mouse. The gray
276 arrows indicate the direction of change in the trial status. **(L)** The projected activity of each area in
277 the CCA dimensions identified. Top, CCA-projected activity in trial 1. Bottom, CCA-projected
278 activity in trial 10. Signals were projected onto pairwise CCA-derived dimensions across brain
279 regions and averaged (n = 3 mice). A typical change of CCA-projected activity for each area is
280 shown in Fig. S5K. **(M)** Each matrix shows normalized correlation coefficients, r, for CCA mode
281 between two of ten trials. A large matrix element value indicates that the source cofluctuated with
282 the target using a similar activity mode; small values imply distinct cofluctuation modes. Results
283 are shown for the largest CCA modes for each source-target pair, averaged over three mice.
284 Solid-outlined boxes highlight areas with lower relevance. Dashed-outlined box indicates stronger
285 correlation between adjacent trials. ***See also*** **Extended Data Fig. 5.**

286 sparse labeling and lack of optical sectioning, restricting depth resolution and the
287 number of neurons sampled[39, 40]. Leveraging Meso2P's large FOV and optical
288 sectioning, we recorded calcium dynamics from densely labeled layer 2/3 neurons
289 (11,941 ± 3,193 neurons; n = 3 mice) during repeated whisker stimulation (Fig. 4A-C),
290 enabling us to directly probe functional connectivity changes within large-scale neural
291 networks with high precision.

292 Single air-puff stimuli triggered widespread, cortex-wide activation across
293 multiple areas (Fig. 4D), where neurons displayed diverse stimulus tuning profiles
294 (Fig. 4E, Extended Data Fig. 5A,B) but with significant co-activation across different
295 areas (Fig. 4F). Population decoding via support-vector machines revealed stimulus
296 presence with > 90% accuracy for 1.5-2 s post-stimulus (Fig. 4G), and accuracy
297 scaled positively with neuron count (Extended Data Fig. 5C,D). Consistently, S1 and
298 V1 contributed more significantly and stably to the overall response pattern (Fig.
299 4H-I), and the stimulus-evoked information was predominantly driven by
300 inter-regional shared fluctuations between S1 and V1 (Extended Data Fig. 5K).

301 Repeated stimuli induced adaptive reorganization of cortical population activity,

302 decreasing calcium event rates and peak spike probabilities across all brain regions,
303 stabilizing after several trials (Fig. 4I, Extended Data Fig. 5E-G). Posterior cortical
304 areas (AP ≈ –3 to –2.5 mm) exhibited advanced response onsets (~ 0.5 s) in later trials,
305 indicating a temporal reorganization (Fig. 4J, Extended Data Fig. 5H,I). CEBRA
306 embeddings of neuronal trajectories showed directional shifts converging onto stable
307 attractors with repeated stimulation (Fig. 4K).

308 Canonical correlation analysis (CCA) revealed region-specific reorganization of
309 neuronal population activity (Extended Data Fig. 5J). Although stimulus information
310 was primarily encoded by locally shared fluctuation patterns between S1 and V1 (Fig.
311 4L, Extended Data Fig. 5K), global coordination across cortical regions emerged
312 during adaptation to repeated stimulation. This global coordination exhibited
313 regionally heterogeneous temporal engagement: Motor cortex (M1), S1, and V1
314 maintained sustained involvement, while the retrosplenial cortex (RSP) underwent
315 rapid reconfiguration during mid-adaptation (Fig. 4M). Critically, analysis of neuronal
316 loading weights across regions demonstrated that adaptive reorganization to sensory
317 stimuli involved not merely changes in network response magnitude, but also
318 restructuring of information transfer architecture within the network. This
319 restructuring was evidenced by directional dynamic changes in unit-specific weights,
320 which were no longer driven by specific local subnetworks but instead reflected
321 global coordinated shifts (Extended Data Fig. 5L,M).

322 Thus, leveraging Meso2P technology, we achieved cortex-wide
323 cellular-resolution recordings at high temporal resolution in densely labeled mice,
324 revealing network-level changes potentially underlying robust perceptual adaptation.
325 Its large FOV design enables high-fidelity, high-throughput spatially extended
326 characterization of functionally distinct cortical regions at mesoscopic scales,
327 facilitating neural network architecture analyses.

328 **Simultaneous dual-layer imaging reveals laminar dynamics during anesthesia**

329 Conscious processing is thought to rely on activity within the cerebral cortex[41-45],
330 whereas general anesthesia induces large-scale cortical network dynamics
331 characterized by widespread neuronal synchrony, particularly involving layers 2/3 and

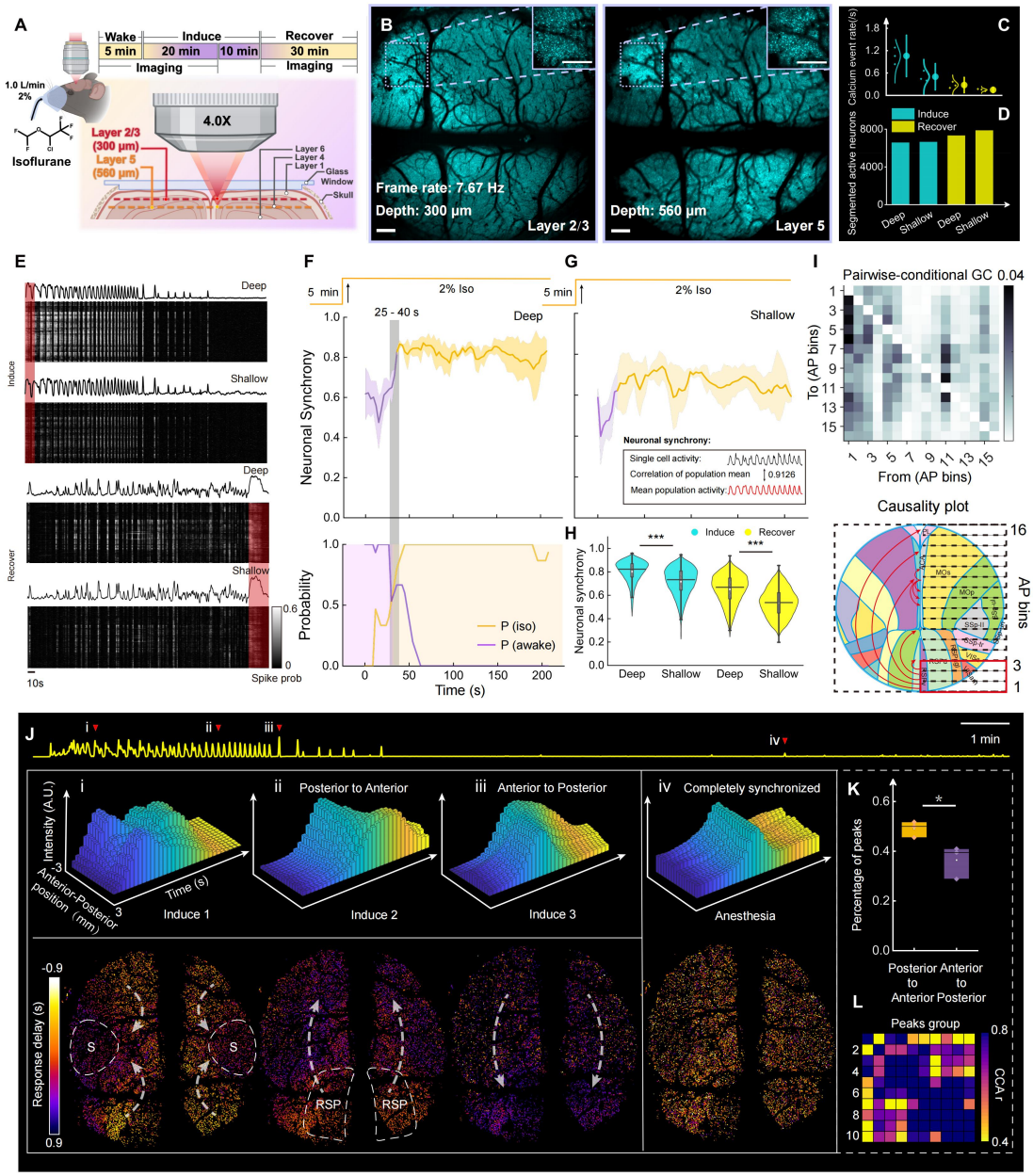

Fig. 5 Cross-laminar recording reveals dynamic signal propagation within and across cortical layers during anesthesia induction. (A) Experimental schematic showing simultaneous two-plane calcium imaging during general anesthesia, with acquisition depths at 300 μm (cortical layer 2/3) and 560 μm (layer 5). **(B)** Representative two-plane imaging examples acquired simultaneously at dual depths, with zoom-in views showing neurons in the same cortical area at both depths. **(C)** Mean calcium event rates of all tracked neurons across different periods and depths, calculated from the initial 3-minute window per period (n = 3 mice). Error bars represent 95% confidence intervals. **(D)** Bar plot of the average number of segmented active neurons across different periods and depths. **(E)** Spike probabilities in a representative mouse. Black trace, averaged signals. Red bands, state transition periods. **(F-G)** Neuronal synchrony of all tracked neurons. Top, anesthesia protocol. Middle, neuronal synchrony in 15-s rolling window. Bottom, probability of mouse being in various states. Purple shading indicates P(awake) > P(iso); yellow shading indicates P(iso) > P(awake). Gray vertical bar marks crossing of these states. Data shown

346 as mean ± SD across n = 3 mice. **(H)** Violin plot of neuronal synchrony across different periods
347 and depths (n = 21387 active cells from three mice). ***$p < 0.001$; Tukey test. **(I)** Top, Granger
348 causality matrix across 16 cortical bins during anesthesia. First column shows causality from the
349 most posterior bin to other bins. Causality with $p < 0.05$ (Granger F test) was shown after
350 correction for multiple comparisons to control false discovery rate. Bottom, summary map of
351 causality between cortical bins. Red arrows indicate inferred causality direction. **(J)** Schematic of
352 synchronized signal propagation direction in a representative mouse. Top, mean spike probabilities
353 during anesthesia induction. Red arrows indicate synchronized spikes expanded in the middle and
354 bottom panels. Middle, bar plots of normalized neuronal spike probability across
355 anterior-posterior positions, showing peak timing sequences in four synchronized events. Bottom,
356 single-neuron-resolution response delay map. Neurons are color-coded by their peak time relative
357 to population activity. (Yellow: early-peaking source regions; purple: late-peaking target regions).
358 Full replication in mice shown in Fig. S5C (n = 3 mice). **(K)** Boxplot of signal propagation
359 direction. For each detected synchronized event, peak timing differences were computed between
360 anterior (8 bins) and posterior (8 bins) regions, then averaged to determine information flow (n = 3
361 mice), *$p < 0.05$, Tukey test. **(L)** Heatmap of normalized CCA mode correlation matrices between
362 consecutive synchronized event clusters, revealing gradual reorganization of neuronal ensemble
363 activity patterns during anesthesia. ***See also*** **Extended Data Fig. 6, Supplementary Video S4.**

364 5. Notably,synchrony changes in layer 5 neurons are temporally aligned with the loss
365 and recovery of consciousness[41-45]. Capturing this phenomenon across multiple
366 cortical layers simultaneously, at cellular resolution and mesoscale coverage, remains
367 challenging with existing approaches.

368 Using Meso2P, we performed simultaneous mesoscale imaging of layers 2/3 and
369 5 in head-fixed, isoflurane-anesthetized mice, with imaging planes at ~ 300 μm and ~
370 560 μm below the cortical surface covering prefrontal and posterior cortices (Fig.
371 5A-B). Throughout both induction and recovery phases, the system reliably captured
372 large populations of active neurons from both layers with high signal fidelity (Fig.
373 5C-D). Notably, both layers exhibited prominent large-scale synchrony across
374 millimeter-scale regions during anesthetic induction (Fig. 5E)—consistent with
375 previous studies[45-48]—with this effect being particularly pronounced in layer 5 (Fig.
376 5F-H). Unexpectedly, leveraging Meso2P's cross-layer, high-speed and large-scale
377 imaging capability, we observed asynchronous information flow within global
378 synchronization events: individual "synchronous" events contained distinct
379 spatiotemporal origins and propagation pathways, with near-complete global
380 synchrony emerging only during late anesthesia. Granger causality analysis revealed a

381 predominant posterior-to-anterior directional bias during induction (Fig. 5I). To
382 validate this finding, we analyzed the spatiotemporal sequence of individual
383 synchronized events by aligning normalized calcium activity across 16 contiguous
384 cortical windows within a ± 2 s window centered on peak activation (Fig. 5J,
385 Extended Data Fig. 6A,B). Although activity appeared globally synchronized,
386 consistent temporal offsets revealed heterogeneity in initiation sites and propagation
387 trajectories. As anesthesia deepened, this variability progressively diminished, with
388 Layer 5 neurons achieving near-complete synchronization exclusively during
389 late-stage events (Fig. 5J, Extended Data Fig. 6B,C). Quantitative analysis of spike
390 onset distributions confirmed posterior-to-anterior propagation as the dominant
391 direction (Fig. 5K).

392 CCA analysis further revealed progressive divergence in global synchrony
393 patterns and substantial reconfiguration of neuronal loading weights across trials (Fig.
394 5L; Extended Data Fig. 6D).

395 Dual-layer imaging also allowed direct interrogation of interlaminar interactions.
396 Activity predominantly propagated in a bottom-up manner from layer 5 to layer 2/3 (p
397 < 0.005), with occasional bidirectional interactions (Extended Data Fig. 6E,F).

398 In summary, these findings show that anesthesia-induced cortical synchrony
399 emerges primarily in deep layers and propagates in a posterior-to-anterior and
400 bottom-up fashion, accompanied by dynamic reconfiguration of interlaminar
401 interactions—significantly departing from the minimal delay synchronization
402 proposed in prior studies[41-45]. With its capability for high-speed, high-precision,
403 large-scale and multi-layer free imaging, Meso2P exhibits unique potential for
404 elucidating information propagation mechanisms within macroscopic cortical
405 networks. This provides novel perspectives for investigating laminar organization
406 during anesthesia and other altered states of consciousness.

407 **Dynamic monitoring of MNP distribution and vascular occlusion *in vivo***

408 Micro- and nanoplastics (MNPs) have rapidly become widespread environmental
409 contaminants, increasingly detected in human tissues including the brain[49].
410 Conventional analytical methods (e.g., Py-GC-MS, Raman imaging) quantify MNPs

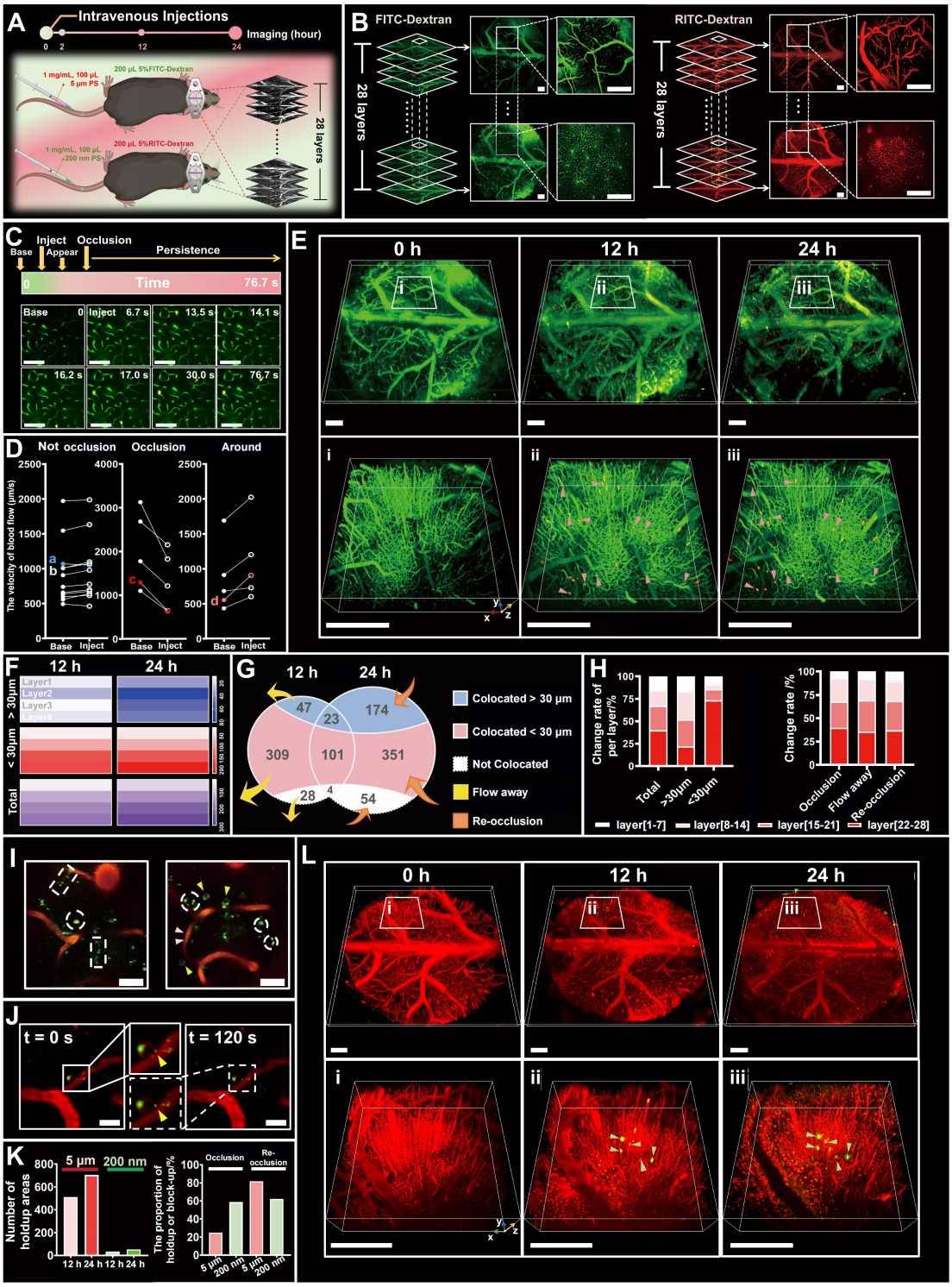

Fig. 6 Dynamic monitoring of MNP distribution and vascular occlusion in the living brain. **(A)** 28-layer MNP imaging in head-fixed mice using Meso2P. **(B)** Vascular resolution in 28-layer Meso2P imaging: FITC-Dextran (green) and RITC-Dextran (red) labeled vessels. **(C)** Distribution pattern of 5-μm MPs in the brain after injection: vessels (green), MPs (red), co-localization (yellow). **(D)** MP distribution at different time points in volumes of 6,000 × 6,000 × 450 μm³ (top) and 1,600 × 1,600 × 450 μm³ (bottom): vessels (green), MPs (red), co-localization (yellow), co-localized MPs observed at both time points (pink arrows). **(E)** Comparison of blood flow velocity in MP-treated vessels; data sources a-d shown in Fig. S7B. **(F)** Depth distribution of MPs

in vessels of different diameters across cortical layers 1–4 (top to bottom) at two time points. **(G)** Spatiotemporal distribution of MPs in vessels of different diameters at two time points. **(H)** Turnover rates of MPs across layers, and proportions of occlusion, clearance, and re-occlusion between layers. **(I)** Distribution pattern of 200-nm NPs in the brain after injection: NPs adhering to vascular walls (pink arrows), within NP-laden cells (yellow arrows), extravascular distribution (white dashed circles), and occluding vessels (white dashed rectangles); vessels (red), NPs (green). **(J)** NP uptake by NP-laden cells: pre-uptake (white solid line) and post-uptake (white dashed line) position comparison (yellow arrows). **(K)** NP distribution at different time points in volumes of 6,000 × 6,000 × 450 μm³ (top) and 1,600 × 1,600 × 450 μm³ (bottom): vessels (red), NPs (green), co-localization (yellow), co-localized NPs at both time points (green arrows). **(L)** Comparison of vascular occlusion between MPs and NPs. *Scale bars*: 500 μm (B, D, K); 100 μm (C); 20 μm (I, J). ***See also* Extended Data Fig. 7 and Supplementary Videos S5-9**

but lack temporal resolution, limiting their use in dynamic biological studies[50]. Standard two-photon microscopy, constrained by its small imaging field, also struggles to capture real-time, three-dimensional MNP distribution and cerebrovascular interactions.

We leveraged Meso2P's large-FOV volumetric imaging to first delineate cortical vasculature of C56BL/6J mice recovered from surgery with vascular dyes (Extended Data Fig. 7A), then dynamically tracked fluorescent 5-μm microplastics (MPs) and 200-nm nanoplastics (NPs), revealing their distinct spatiotemporal accumulation patterns and cerebrovascular consequences (Fig. 6A,B).

MPs entered cortical vessels rapidly (~ 13 s post-injection), causing immediate vascular occlusions (Fig. 6C, Supplementary Video 5). Occluded vessels exhibited reduced blood flow, compensated by increased flow in adjacent vessels (Fig. 6D; Extended Data Fig. 7B). Compared to the 12-hour time point, partial vascular occlusions were resolved by 24 hours, while some persisted for at least 12 hours (Fig. 6E). MPs preferentially accumulated in smaller vessels (< 30 μm diameter), particularly within deeper cortical layers, and either persisted or re-occluded after partial clearance (Fig. 6F-H, Extended Data Fig. 7C, Supplementary Video 6).

In contrast, smaller-sized NPs diffused broadly upon vascular entry, forming diverse aggregates (granular, aggregated, and cellular) within vessels and surrounding tissues (Fig. 6I, Extended Data Fig. 7D, Supplementary Video 7). NPs adhered to vascular walls, occasionally extravasated, and progressively accumulated within

453 putative phagocytes with time-dependent increase ("NP-laden cells", Fig. 6J,
454 Extended Data Fig. 7E, Supplementary Video 8). NP-induced vascular occlusions,
455 though fewer, were notably persistent (~ 60% unresolved; Fig. 6K,L). Vessel wall
456 adhesion promoted recurrent clustering, stabilizing occlusions despite NPs' small size
457 (Extended Data Fig. 7F, Supplementary Video 9).

458 Thus, Meso2P offers a powerful platform for dynamic, cellular-resolution
459 analysis of complex *in vivo* processes. Its volumetric imaging capacity captures
460 three-dimensional particle distributions and biological responses in real time, enabling
461 new investigations into a wide range of questions that demand large-scale,
462 three-dimensional coverage.

463 Discussion

464 Meso2P resolves a long-standing optical bottleneck in two-photon microscopy
465 by physically separating excitation and detection, effectively breaking the inverse
466 relationship between numerical aperture and FOV. A compact paraboloid collector
467 boosts the effective detection NA to 0.87, while excitation remains delivered through
468 a standard 4× objective. As a result, diffraction-limited performance is maintained
469 uniformly across a contiguous 6 × 6 mm^2 imaging window, avoiding the use of
470 oversized custom optics. This innovative approach converts high-NA collection from
471 a mechanical limitation into a flexible optical design choice.

472 The volumetric implementation pushes single-beam point scanning toward its
473 physical limits. Time-division multiplexing increases the effective laser repetition rate
474 from 80 MHz to 320 MHz, remaining just below the 3.125-ns fluorescence lifetime of
475 common calcium indicators, thus minimizing inter-plane crosstalk. Piezo-driven axial
476 stepping distributes excitation pulses across a 520-μm depth range at 1 Hz. The
477 resulting 6 × 6 × 0.5 mm^3 imaging volume optimally balances sampling density, tissue
478 heating, and indicator kinetics. Achieving greater imaging speed would likely
479 necessitate parallel excitation approaches, potentially compromising resolution and
480 signal fidelity in scattering tissues. Crucially, Meso2P's modular design—comprising
481 lateral collection, volumetric imaging, and holographic stimulation modules—allows

482 users to flexibly adapt the instrument according to experimental requirements and to
483 incorporate additional functionalities as imaging technologies evolve.

484 Handling the data rate of cortex-wide imaging motivated the development of
485 NeuroPixelAI. By streaming registration, frame-wise deep denoising and
486 region-adaptive segmentation through memory-aware kernels, the pipeline processes
487 full-session files on a single workstation and returns spike trains with higher
488 segmentation and inference fidelity than widely used alternatives. Its open-source
489 code base and modular design invite adoption of new models as they appear and
490 lower the barrier for laboratories that lack extensive computational expertise.

491 Although we primarily demonstrated Meso2P's capabilities through
492 neuroscience applications, its optical core is versatile and equally suited to imaging
493 dynamic biological processes such as immune-cell trafficking, tumor-stromal
494 interactions, or embryonic morphogenesis, wherever large-scale coverage with
495 single-cell resolution is required.

496 Several limitations remain. The 11.7-µm axial point-spread function approaches
497 the diameter of a cortical soma, so applications that demand sub-laminar separation
498 will still benefit from high-NA objectives. The collector sits above the cranial window
499 and currently precludes integration with head-mounted devices, which will require
500 miniaturisation or fold-mirror designs. The 3.125-ns inter-plane delay is a
501 compromise between crosstalk and multiplexing depth; extending it to six
502 nanoseconds would sharpen temporal separation but halve the number of
503 simultaneous planes. NeuroPixelAI analyses each imaging plane independently; a
504 fully three-dimensional model could further improve source separation in densely
505 labeled tissue. Finally, while we confirmed accurate co-registration of imaging and
506 holographic stimulation, we did not explore closed-loop perturbations, leaving ample
507 scope for future circuit manipulation experiments.

508 Collectively, Meso2P demonstrates that decoupling fluorescence detection from
509 excitation is a powerful strategy to achieve NA-limited performance across mesoscale
510 FOV. Its modular hardware–software architecture provides a reproducible and flexible
511 framework for next-generation instruments aimed at comprehensive imaging,

perturbation, and analysis of biological activity across extensive cortical volumes in real time.

Methodological Details

Animals

All mouse experiments were approved by the Institutional Animal Care and Use Committee of the Department of Laboratory Animal Science, Fudan University, Shanghai, China (ethical approval no. 2022JSITBR-013). Mice were housed in a controlled environment (~ 20 °C, 45% relative humidity) under a 12 h light/dark cycle (lights on 08:00, off 20:00). Unless specified, both male and female mice transgenically expressing GCaMP6s in excitatory neurons (*Camk2α-Cre*, Cyagen Biosciences #C001015 × *fl-GCaMP6s*, Jackson Labs #031562) underwent cranial window implantation at 8-10 weeks. Briefly, under 1.5% isoflurane (RWD Life Science #R510-22-10) anesthesia (mixed with oxygen), craniotomy was drilled (7 mm). The skull flap was removed while preserving meningeal integrity. After debris clearance, a cranial window (6.5-mm coverslip bonded to a glass ring: 7.5-mm outer diameter, 6-mm inner diameter) and a metal headpiece fixed with dental cement/cyanoacrylate glue were implanted. Mice with major intraoperative hemorrhage were excluded. After 2-week recovery (daily dexamethasone, Beyotime Biotechnology #C001015 and cefazolin, Shanghai Macklin Biochemical Technology #HY-B0712A, 5 mg/kg, i.p.), mice were adapted to head fixation for 2 weeks before imaging. Unless specified, head-fixed imaging used a parabolic lateral collection module and custom 4× objective. At the end of the experimental procedures, unless specified, experimental animals were euthanized by CO_2 asphyxiation followed by cervical dislocation. Neuronal imaging signal extraction was performed using NeuroPixelAI.

System Configuration

Laser Source

The laser system consisted of two components: an imaging laser source and a photostimulation laser source. For imaging, we employed the Chameleon Discovery

541 NX laser system (Coherent, Inc.), which features a tunable wavelength range from
542 660 nm to 1,320 nm, a pulse duration of 100 fs, and a repetition rate of 80 MHz. At a
543 wavelength of 920 nm, the system delivers an average output power of 3,200 mW.
544 First, we used the laser's integrated dispersion compensation module to generate an
545 anomalous group delay dispersion (GDD) of -17,358 fs^2, compensating for material
546 dispersion from system components. We then adjusted the laser output power using a
547 rotatable half-wave plate (AHWP05M-980, Thorlabs) combined with a polarizing
548 beam splitter (PBS255, Thorlabs), equipped with a precision rotation mount (PRM1)
549 and a voice coil motor controller (KVC101, Thorlabs). For photostimulation, we used
550 a Monaco 1035 laser system (Coherent).

551 **Spatiotemporal Multiplexing Module**

552 To increase the system's sampling rate to 320 MHz, thus reaching the sampling
553 limit for fluorescence imaging, we constructed a polarization-based spatiotemporal
554 multiplexing system (Extended Data Fig. 2A,B). The system initially divides the
555 incident light into four beams using a combination of three polarizing beam splitters
556 (PBS623, LBTEK) and half-wave plates (HWP25-905A-M, LBTEK). Each half-wave
557 plate is mounted on a rotatable adjustment frame (CRM-1AS) to control power
558 allocation among the optical paths. Each optical path was then assigned a distinct time
559 delay, resulting in the sequential emission of the four light beams at 3.125 ns intervals.
560 Furthermore, the system incorporated a pair of cemented lenses (AC250-150-B-ML
561 and AC250-300-B-ML, Thorlabs) arranged as a magnification telescope. This
562 arrangement enabled beam enlargement while allowing focal position adjustment
563 using a precision translation stage (A-LSQ-E, Zaber), thereby creating four adjustable
564 focal points on the imaging plane. Finally, the optical paths were combined using two
565 beam splitters (BS1255-B, LBTEK) and a polarizing beam splitter, producing a
566 composite light beam characterized by a 320 MHz sampling frequency, 3.125 ns
567 temporal intervals, and a 130 μm spatial separation between focal points. The power
568 of each beam within the composite light and the spacing between focal points could
569 be adjusted via the corresponding half-wave plates and by moving the lenses on the
570 translation stage, respectively, to meet varying imaging requirements.

571 **Excitation Optical Pathway**

572 The excitation optical pathway of Meso2P is shown in Fig. 1A and Extended Data
573 Fig. 1B,D. The optical path begins with a Y-axis scanning galvanometer mirror
574 (6215H, Cambridge Technology) at the system forefront. The beam then passes
575 through a telescope comprising of two telecentric flat field scanning lenses
576 (LSM54-850, Thorlabs) before being incident on a resonant mirror (CRS8K,
577 Cambridge Technology) for X-axis scanning. This separated-axis design prevents
578 sampling depth changes from affecting the XY field of view (FOV). After the
579 scanning process, the beam undergoes aperture magnification through a 3.4x
580 magnification telescope composed of a telecentric flat field scanning lens
581 (LSM54-850, Thorlabs) and two doublet achromatic lenses (AC508-300-B), followed
582 by a custom aberration compensation module before entering the rear aperture of the
583 objective lens.

584 **Aberration Compensation Module**

585 In Meso2P, most optical modules employ commercial low-aberration components,
586 but cumulative aberrations from optical mismatches still significantly degrade image
587 quality. To correct multiple types of aberration present in the system and enhance the
588 fluorescence excitation efficiency, we designed a symmetric cemented lens pair with
589 large air gaps, inspired by the Petzval lens structure. This pair of lenses, after design
590 optimization, features an extended focal length as given by:

591 $$\phi = \phi_1 + \frac{h_2}{h_1}\phi_2 \quad (1)$$

592 here, ϕ_1 and ϕ_2 represent the focal powers of the front and rear lens groups,
593 respectively, and ϕ denotes the total focal power of the module. This design allows
594 for significant optimization of spherical aberration, field curvature, and astigmatism
595 without affecting the original focal position of the system. The design primarily
596 focuses on optimizing the flatness of the imaging field quality, ensuring that the
597 overall composite aberration RMS across the imaging field remains within 0.1 ± 0.01
598 λ at the operational wavelength of 920 nm ± 18 nm.

599 **Parabolic lateral collection module**

The parabolic lateral collection module consists of six components: a parabolic reflector module, a first focusing lens (LA1145-A, f = 75 mm, Thorlabs), a filter cube module (including custom-sized low-pass filter ET720sp-2p8, high-pass filter T556lpxs-UF3, and band-pass filters for red and green wavelengths ET605/70m and CT512/60bp, Chroma Technology), a second focusing lens, a third focusing lens (48-244-INK, f = 50 mm, Edumund), and a photomultiplier module (H13543-300, HAMAMATSU) (Fig. 1D and Extended Data Fig. 1G).

Due to the constraints imposed by the aperture of optical components, the imaging field of view (FOV), and the focal length of the objective, the parabolic reflector module was meticulously designed (Extended Data Fig. 1H). The focal length p and the distance behind the focus L are subject to the following limitations:

$$\begin{cases} f_{\text{obj}} < 33\text{mm}: p < 33, \\ W_{\text{laser}} = 8\text{mm}: p > 8, L > 4, \\ D_{\text{Rlens}} = 52\text{mm}: y(p + L/2) < 26. \end{cases} \tag{2}$$

Furthermore, to ensure that the fluorescence collection efficiency is nearly uniform across different points on the imaging plane, the distance before reflection along path 1 should be relatively long, necessitating a maximally large p. Additionally, to enable the collection module to gather fluorescence at larger angles, the angle θ along path 2 should be relatively small, which requires L to be maximally large while keeping p as small as possible. A grid search method was employed to balance these constraints, ultimately selecting the module parameters p = 20 and L = 8.

Given the absence of commercially available 4× long-working-distance objectives suitable for large-field multiphoton fluorescence imaging with a working distance greater than 30mm, a custom objective lens was designed and fabricated to accommodate the parabolic lateral collection module (Fig. 1B and Extended Data Fig. 1G). This objective uses a five-group, seven-element design, equipped with an M32 × 0.75 thread, and is mounted on a piezo objective scanner (PFM450E, Thorlabs), allowing for independent axial scanning. The objective has a focal length f = 45 mm, a numerical aperture NA = 0.296, and a working distance of 31 mm. Targeted optimizations were performed to minimize spherical aberration, astigmatism, and meridional field curvature, ensuring that the composite wavefront aberration RMS

across the entire field at the operational wavelength of 920 nm remains below 0.02 λ. Using Zemax-based optical system simulations, this lens approaches the performance of an ideal objective. Notably, due to the customizable structure of the self-designed objective, adjustments were made during simulation to further enhance image quality, aligning the lens optimally with the system.

Multiplexed Acquisition of Quadruple Electrical Signals

Due to the frequency limitations of the data acquisition card (vDAQ, MBF Bioscience), the maximum signal acquisition rate of the system is constrained to 80 MHz. To facilitate the sampling of a 320 MHz electrical signal using this acquisition card, a strategy involving the multiplexed acquisition of quadruple electrical signals was implemented. During the imaging process, the fluorescence signal is first converted into an electrical signal by a photomultiplier tube (PMT, H7422-40, Hamamastu), which is then amplified by an amplifier. The output from the amplifier (C9663, Hamamastu) is fed into a four-way power splitter (PD-0/6-4S, TD-MICROWAVE), which divides the signal into four pathways. To achieve temporal displacement among the multiple acquisition points, different cable lengths are used based on the rate of electrical transmission through the conductor. This arrangement allows the four separate channels of the acquisition card to capture the four components of the 320 MHz signal sequentially. The difference in cable lengths can be estimated using the following equations:

$$v = \frac{1}{\sqrt{\varepsilon_0 \varepsilon_r \mu_0 \mu_r}} \tag{3}$$

$$\Delta L = v \cdot \Delta t \tag{4}$$

where ε_0 is the permittivity of free space, 8.89×10^{-12} F/m8, ε_r is the relative permittivity of the material, μ_0 is the permeability of free space, $4\pi \times 10^{-7}$ H/m, μ_r represents the material's relative permeability, and Δt is 3.125 ns.

Denoising Algorithm Testing

To evaluate the performance of various denoising algorithms, we compared their effects on data with a 0 dB signal-to-noise ratio (SNR) across different frame rates (Extended Data Fig. 4B), where SNR is defined as the ratio of signal power to noise

power:

$$\mathrm{SNR} = 10lg\frac{P_{\mathrm{S}}}{P_{\mathrm{N}}} \tag{5}$$

where P_{S} represents the signal power, and P_{N} denotes the noise power.

We first acquired clean calcium imaging videos at 100 Hz frame rate, 200 μm depth, and 300 × 300 μm² FOV using NAOMI[51]. These datasets were then downsampled to generate frame rates spanning 1-30 Hz, followed by noise injection to simulate experimental conditions. The noise inherent in calcium imaging data predominantly consists of photon shot noise, dark current noise, and readout noise[52]. Among these, readout noise is characterized by a Gaussian distributio and the power of dark current noise is relatively low and stable[53]. The principal component of noise, however, is the unavoidable shot noise, which occurs due to quantum fluctuations during the photon acquisition process and is also known as Poisson noise. The theoretical noise model can thus be described as:

$$I_{\mathrm{acq}} = P(I_{\mathrm{clean}}) + N(0, \sigma^2) \tag{6}$$

Considering digital resolution (image bit depth), the generation of MPGnoise can be reformulated as:

$$I_{\mathrm{acq}} = \mathrm{MPG}(I_{\mathrm{clean}}; Q, n, \sigma^2) = \frac{2^n-1}{Q} * P(\frac{I_{\mathrm{clean}}*Q}{2^n-1}) + N(0, \sigma^2) \tag{7}$$

here, I_{clean} represents the photon distribution in the pristine data, and I_{acq} represents the corresponding noise-contaminated photon distribution. P is a function operator of the signal-related Poisson noise, N represents signal-independent zero-mean Gaussian noise with a variance characteristic σ^2, n denotes the bit depth of the captured image (set here as n = 16), MPG(·) is the operator generating MPG noise, used to simplify the mathematical expression and Q represents the relative number of photons per pixel captured by the detector. In this work, different Q values were used to simulate calcium imaging data with various SNRs. Given that Gaussian noise constitutes a smaller component of the total noise, its mean is set to zero, and its variance is set to σ^2 = 1000, hence σ = 31.623.

To calculate SNR in calcium imaging videos, for a noise-free calcium imaging

video, we calculate the signal power by squaring the intensity of each pixel in every frame throughout the video and then dividing by the total number of pixels. This can be expressed specifically as:

$$P_{\mathrm{s}} = \sum_{\mathrm{pixs}} \frac{I^2}{\mathrm{pixs}} \tag{8}$$

where I represents the pixel value of a single pixel in a particular frame, and pixs is the sum of the number of pixels across all frames. After calculating the signal power, similarly, the noise power is determined by computing the squared difference between the pixel values of the noisy video and the noise-free video at each point, summed and then divided by the number of pixels:

$$P_{\mathrm{N}} = \sum_{\mathrm{pixs}} \frac{(I - I_n)^2}{\mathrm{pixs}} \tag{9}$$

where I_n denotes the pixel value in the noisy video for a single pixel in a particular frame. Finally, the SNR is calculated according to Equation (5).

Assessment of Cell Segmentation Algorithms

Neuronal spatial segmentation is typically framed as a multi-class task, assigning each pixel to its corresponding neuron. To evaluate algorithm performance, we used standard metrics: Precision, Recall, and the F1 Score (Extended Data Fig. 4D-F). Furthermore, the computational speed of the segmentation algorithms was included as a performance benchmark.

Precision, also known as positive predictive value, represents the proportion of true positives among the samples predicted as positive. It can be described by the following equation:

$$\mathrm{Precision} = \frac{\mathrm{TP}}{\mathrm{TP+FP}} \tag{10}$$

where TP is true positive, FP is false positive.

Recall, also referred to as sensitivity, indicates the proportion of true positives out of all actual positive samples. It can be represented as:

$$\mathrm{Recall} = \frac{\mathrm{TP}}{\mathrm{TP+FN}} \tag{11}$$

where FN is false negative.

The F1 Score, which emerges from the concepts of Precision and Recall,

typically presents a trade-off between these metrics: high Precision often coincides with lower Recall, and vice versa. To provide a balanced consideration of these metrics, the concept of the F1 Score was introduced:

$$F1 = \frac{2*\text{Precision}*\text{Recall}}{\text{Precision}+\text{Recall}} \tag{12}$$

Regarding the processing speed of the algorithms, we have simply evaluated it in frames per second.

The specific method of testing employed cross-validation. In the experimental setup, we used six sets of calcium imaging videos at 3.51 Hz with 6,500 frames (512 × 512 pixels), manually annotating nearly 600 ROIs as ground truth using Cellpose 2.0. For algorithms requiring network training, five sets of data were used for training and the remaining set served as the test set, completing the evaluation across all six video sets in a repetitive manner. For algorithms that did not require training, parameter adjustments were made prior to testing. During each algorithm's testing phase per video set, we concurrently recorded Precision, Recall, F1 Score, and image processing speed as metrics of evaluation.

Baseline Correction Algorithm

In certain experiments, we observed a concurrent reduction in neuronal action potential firing and total $[Ca^{2+}]_i$ fluctuations, manifesting as baseline variations in the recorded data. To accurately extract spikes from individual neurons despite ongoing baseline fluctuations, we incorporated a baseline correction algorithm based on Cubic Spline Approximation (Smoothing) (csaps) into our software. Upon inputting data, the smoothing parameter of csaps is adjusted to smooth = 1e-8. The data fitted using this method serve as the baseline for calculating the change in neuronal fluorescence, $\Delta F/F0$:

$$\text{dff}_{\text{sig}} = \frac{\text{raw}_{\text{sig}}\text{-baseline}}{\text{baseline}} \tag{13}$$

where baseline is the baseline obtained by fitting the original data using the csaps algorithm, raw_{sig} represents the original data, and dff_{sig} denotes the final calculated change in neuronal fluorescence intensity $\Delta F/F0$.

742 **Spike inferrence Algorithm Testing**

743 To evaluate algorithm performance, we computed the Pearson correlation
744 coefficient between electrophysiologically recorded membrane potentials and inferred
745 spike trains from original calcium imaging data processed by each algorithm.
746 Analyses were performed across multiple standardized noise levels (Extended Data
747 Fig. 4H-J).

748 Specifically, each algorithm processed original calcium signals to generate
749 inferred spike probability time series. These inferred traces were then compared to
750 simultaneously recorded membrane potential signals, which were converted into
751 standardized spike probability estimates using established methods. Correlation
752 coefficients served as the primary metric to: (1) compare algorithm performance
753 across different standardized noise levels, and (2) assess the stability of each
754 algorithm's performance at a fixed noise level.

755 The definition of standardized noise level is given by[54]:

756 $$\upsilon = \frac{\sigma_{\Delta F/F}}{\sqrt{f_{\mathrm{r}}}} = \frac{Median_t|\Delta F/F_{t+1} - \Delta F/F_t|}{\sqrt{f_{\mathrm{r}}}} \quad (14)$$

757 here, based on optical imaging principles with finite granularity noise where the
758 detector collects N photons per second, the noiae magnitude is $\sqrt{N}$. Thus, the
759 baseline noise level is expressed as: $\sigma = \frac{1}{\sqrt{N}}$ (in percentage units). Considering the
760 frame rate, f_{r}, for each frame, the formula's N can be replaced entirely by N/f_{r},
761 resulting in a baseline noise level per frame of: $\sigma_f = \frac{\sqrt{f_{\mathrm{r}}}}{\sqrt{N}}$. To eliminate the factor of
762 frame rate, the standardized noise level υ is defined as the Equation (14).

763 To convert the potential signals into spike probabilities, we performed
764 binarization followed by Gaussian kernel convolution. The original spike timing data
765 in Fig. 3F and Extended Data Fig. 4H show discrete signals. After binarization and
766 convolution processing, the resulting spike probabilities are used to evaluate the
767 performance of the algorithms.

768 **Iterative Correlation Sorting Algorithm**

769 Even in the absence of recorded specific stimulus times during experiments,
770 neuronal signals can be sorted by their inherent temporal characteristics of local firing
771 potentials. Initially, the data from all neurons are aggregated into a single time series
772 (representing the overall temporal signal of all neurons). The100 largest-amplitude
773 time points from this series as template for cross-correlation-based alignment of all
774 neuronal signals. Subsequently, the average of the top 10 most highly correlated
775 neuronal signals post-alignment is taken as the new template to reorder all neuronal
776 signals. After 30 iterations, the resulting correlation sorting plot appears in the
777 lower-right image frame of software Tab 2.

778 **Development and Implementation of NeuroPixelAI for Large-Field Image**
779 **Analysis on a High-Efficiency Software Platform**

780 In order to address the challenges associated with processing extremely large
781 image datasets from wide-field observations and to furnish a platform capable of
782 one-click, high-speed processing, we developed NeuroPixelAI using PyQt5. The
783 workflow is compartmentalized into six distinct stages: motion registration, image
784 denoising, cell segmentation, signal extraction (baseline correction), spike inference,
785 and correlation-ranking clustering. Given the dynamic changes inherent to biological
786 activity, tissue expansion, and mechanical fixation during imaging processes, there
787 often occurs displacement within the imaging field. To counteract this, our initial step
788 involves motion registration. We adopted a phase-correlation-based registration
789 method, similar to that used in Suite2p[26], which iteratively computes the average of
790 the most correlated frames in a video to serve as a reference image. Subsequent
791 frames are then aligned with this reference image to achieve motion registration. We
792 enhanced this algorithm by incorporating dynamic memory allocation, allowing it to
793 handle larger data structures effectively. Moreover, we reduced the adjustable
794 parameters from twenty to four input parameters, and introduced options for non-rigid
795 registration and bidiphase adjustment, significantly reducing parameter redundancy
796 and simplifying usability. The second step is image denoising. Calcium imaging data,
797 due to the transient, low-amplitude accumulations of intracellular calcium ions and

798 the rapid dynamics involved, coupled with the limitations of electronic detection
799 equipment, are susceptible to various types of noise contamination, such as shot noise,
800 dark current noise, and readout noise[53]. This poses significant challenges for
801 high-performance imaging, such as dendritic imaging and deep tissue imaging. We
802 referred to algorithms such as DeepCAD-RT[29] and SRDTrans[30] (Extended Data Fig.
803 4B,C), which are known for their speed, precision, and parameter-free operation.
804 Upon completion of their training phase, these algorithms can effectively eliminate
805 various types of white noise from multiphoton image data. Consequently, we
806 integrated the denoising function with the prior motion registration into a unified
807 module (Image Enhancement) within NeuroPixelAI and included visualization
808 capabilities. The third step involves cell segmentation. To effectively handle the
809 diverse cellular morphologies and distributions across different brain regions and to
810 facilitate efficient one-click processing, we developed an optimized processing
811 pipeline. Building upon Cellpose 2.0[55], we implemented parameter optimization and
812 established a region-adaptive framework to achieve high-precision, high-throughput
813 cellular segmentation across large fields of view. The streamlined workflow enables
814 efficient one-click processing within NeuroPixelAI, while retaining manual curation
815 capabilities for user-guided refinement. Algorithm performance was validated against
816 multiple alternatives (CNMF-E[27, 56], Cellpose[26, 55], SUNS[57]) using both raw and
817 denoised data (Extended Data Fig. 4D-F). The fourth stage in our methodology is
818 signal extraction. Based on the cellular masks generated during the third stage of cell
819 segmentation, we sum the pixel values within each ROI in every frame to obtain the
820 raw temporal data of individual neurons. Additionally, we offer an optional baseline
821 correction method utilizing the cubic spline interpolation algorithm. This approach is
822 designed to correct baseline fluctuations in the signals, which may arise due to
823 changes in the concentration of optical indicators within cells, photobleaching, or
824 specific biological activities (Extended Data Fig. 4G). This method is particularly
825 advantageous for subsequent spike inference during extended recordings of multiple
826 signals. The final stage involves spike inference. Commonly used optical imaging
827 signals, particularly calcium signals, serve as indirect, typically non-linear, and

828 low-pass filtered representations of more fundamental variables of interest—namely,
829 somatic action potentials (spikes)[54, 58-60]. Historically, many studies have analyzed raw
830 calcium signals directly[39, 61] or employed various deconvolution algorithms, such as
831 OASIS (Suite2p, CaImAn)[61-64] or custom-written toolbox[65], to approximate signals
832 closer to the original action potentials for analysis. However, in practical imaging
833 scenarios, the single-pulse responses of different neurons, and even different temporal
834 segments within the same neuron, vary significantly[65]. Moreover, parameters like
835 pulse width, often preset in deconvolution algorithms, are challenging to estimate
836 accurately prior to analysis. This variability leads to substantial standard deviation
837 fluctuations in the precision of traditional deconvolution algorithms, especially when
838 processing data with low SNRs. We tested various deconvolution algorithms[26, 27, 66]
839 and the deep learning algorithm Cascade using datasets provided by CRCNS[31, 32] and
840 to restore calcium signals to electrophysiological signals (Extended Data Fig. 4H-J).
841 Our findings demonstrate that the deep learning-based Cascade algorithm
842 significantly outperforms traditional deconvolution methods when dealing with
843 calcium imaging data of varying SNR levels. We have integrated Cascade's testing
844 methodology into NeuroPixelAI, along with enhancements such as visualization
845 features for neuronal signals during processing and a signal-correlation iterative
846 sorting algorithm (Extended Data Fig. 4K). These enhancements allow for an intuitive
847 observation of the temporal signals and overall correlation characteristics of neurons
848 post-processing.

849 **Instrument (Meso2P) Validation**

850 For in-house bred *Camk2α-Cre::fl-GCaMP6s* mice, imaging comparisons were
851 conducted on the same cortical plane (250-μm depth) without and with the parabolic
852 lateral collection module. Images were acquired in high-speed (2,048 × 2,048
853 pixels/frame, 7.67 Hz) or high-resolution mode (4,096 × 4,096 pixels/frame, 3.83 Hz)
854 using 130-mW excitation power. Fluorescence collection efficiency was assessed
855 using the parabolic lateral collection module at 330-μm depth below the cortex with
856 90-mW imaging power. Twenty-eight-layer volumetric imaging was achieved using
857 parabolic lateral collection, time-division multiplexing, and a piezo-driven z-scanning

858 module. This enabled simultaneous imaging at 2,048 × 2,048 resolution across a
859 6,000 × 6,000 × 500 μm^3 volume (from 60 to 560 μm below the cortical surface) at
860 1.1 Hz with 250-mW excitation power. For 8-10-week-old *Camk2α-Cre::fl-GCaMP6s*
861 mice, the red-shifted opsin pAAV-EF1α-DIO-C1V1(t/t)-Ts-mCherry-WPRE (Obio
862 Technology) , a widely used optogenetic actuator, was injected before cranial window
863 implantation. After a 4-week recovery period for viral expression, two-photon
864 single-cell optogenetic stimulation imaging used 50-ms light pulses every 16 s (10
865 cycles; cycles 4-9 as control) at 220-μm depth (Nikon, 16×/0.8 NA objective).
866 Imaging power: 20 mW; stimulation: 50 mW.

867 **Photodamage Assessment**

868 Uniform 28-layer imaging of 500-μm-thick cortex was performed for 1 h at 0
869 mW (control), 250 mW and 350 mW excitation (parabolic lateral collection module,
870 4× objective). After 20 h, mice were anesthetized with 1% pentobarbital sodium and
871 transcardially perfused with heparinized saline (20 U/mL) followed by 4%
872 paraformaldehyde (PFA). Brains were post-fixed overnight in 4% PFA at 4 °C,
873 cryoprotected 20% and 30% sucrose/PBS, and sectioned at 25-μm thickness.
874 Photodamage was assessed by immunofluorescence: sections blocked in 5% normal
875 donkey serum/PBST (PBS + 0.3% Triton X-100) for 1 h, incubated with primary
876 antibody (HSP70/HSP72 monoclonal antibody, Enzo Life Sciences #ADI-SPA-810,
877 1:400) overnight at 4 °C, and labeled with secondary antibody (Alexa Fluor® 594
878 AffiniPure® Donkey Anti-Mouse IgG (H+L), Jackson #715-585-151) for 2 h at room
879 temperature, and sealed with Antifade Mounting Medium with DAPI (Beyotime
880 Biotechnology #P0131) Six cortical regions per brain were imaged using a confocal
881 microscope. Thermal injury areas were quantified using ImageJ software (v1.53t,
882 NIH)[67] with the "Threshold" function (normalized to 0-mW control). Data analyzed
883 by one-way ANOVA with Tukey's post hoc test (n = 3 mice per group).

884 **Optical resolution calibration.**

885 To calibrate the optical resolution of our multiphoton imaging system, we
886 computed the 1/e intensity radius of the focal spot based on Gaussian functions fit to
887 integral representation of the electric field near the focus of a diffraction-limited

focus[68]:

Lateral radius:

$$\omega_{xy} = \frac{0.31\lambda}{\sqrt{m}NA} \tag{15}$$

Axial radius:

$$\omega_z = \frac{0.266\lambda}{n_i\sqrt{m}\sin^2(\alpha/2)} = \frac{0.532\lambda}{\sqrt{m}}\left[\frac{1}{n_i - \sqrt{n_i^2 - \mathrm{NA}^2}}\right] \tag{16}$$

$\alpha = \arcsin(\mathrm{NA}/\mathrm{n})$ in radians. ω is the 1/e radius. For the $1/e^2$ radius multiply by $\sqrt{2}$. For the FWHM multiply by $2\sqrt{\ln 2} = 1.665$. m = order of excitation: m = 1 for conventional excitation, m = 2 for 2 photon excitation, etc. Experimentally, we imaged 0.1 μm fluorescent beads and derived the 1/e radius from measured FWHM values.

Quantification and statistical analysis

Image Processing and Statistical Analysis

All image data were processed using NeuroPixelAI for motion correction, denoising, cell segmentation, signal extraction, and spike inference, with additional baseline correction and iterative sorting applied based on data characteristics. Outputs include but are not limited to: enhanced images, neuron masks and properties, raw pixel values, ΔF/F0 signals, spike probabilities and inferred spikes. Statistical analyses used MATLAB® R2023a (v9.14.0, Mathworks). Normally distributed continuous data are presented as mean ± s.d. All statistical details (the size and type of individual samples, n) are specified in figure legends.

Cascade Model Training

Given variable imaging rates across experiment, we trained multiple spike-inference models using the "Global EXC" dataset[54] at diverse frame rates and Gaussian smoothing kernel parameters. This dataset covers multiple indicators (e.g., GCaMP6f, GCaMP6s, OGB-1, GCaMP5k, Cal-520, R-CaMP1.07, and jRCaMP) and brain regions (e.g. the visual cortex, somatosensory cortex, hippocampus, several

914 regions of the zebrafish forebrain, and the olfactory bulb), including some inhibitory
915 neurons. The training noise levels ranged from standard noise level υ 2 to 9. The
916 smoothing parameter was empirically set t othe inverse of the frame rate multiplied by
917 1.5; for instance, at 7.67 Hz, the smoothing parameter was 195 ms, and at 30 Hz, it
918 was 50 ms. The causal ground truth smoothing kernel was set to 0 ms.

919 Cortex-wide neuronal dynamics during whisker stimulation

920 Experiment Paradigms

921 An air-puff nozzle was positioned in front of head-fixed
922 *Camk2α-Cre::fl-GCaMP6s mice*. After a 5-min baseline recording, mice received 10
923 cycles of air-puff stimulation (15-s duration each) with 45-s interstimulus intervals.
924 Air-puff delivery was synchronized with imaging using a programmable solenoid
925 valve controller. Neuronal calcium signals at 300-μm depth within a 6,000 × 6,000
926 μm^2 cortical area were continuously recorded with the parabolic lateral collection
927 module (2,048 × 2,048 pixels, 7.67 Hz).

928 Brain Region Division and Regional Neuron Statistics

929 Brain regions were delineated and masks were created referencing the Allen
930 Brain Atlas[69]. Imaging areas were proportionally registered based on coronal and
931 horizontal planes, and all neurons were assigned to brain regions based on centroid
932 coordinates processed by NeuroPixelAI (Fig. 4C and Extended Data Fig. 5A).

933 Definition of Active (Coding) Cells

934 Active neurons were identified based on the inferred spikes output from
935 NeuroPixelAI. Neurons that exhibited an average action potential firing rate more
936 than twice the resting state firing rate of mice during ten stimulus trials were
937 considered "active". Under Gaussian distribution, non-coding neurons should have a
938 95% probability of firing at less than twice the resting rate in a single experiment (Fig.
939 4E and Extended Data Fig. 5C,D).

940 $$P\left(\mu - 1.96 \times \frac{\sigma}{\sqrt{n}} \leq \bar{x} \leq \mu + 1.96 \times \frac{\sigma}{\sqrt{n}}\right) = 0.95 \quad (17)$$

941 Decoding Neural Population Activity Using SVM Decoders

942 To investigate the encoding responses of neural population activity in various

943 brain regions to air puff stimuli, we employed SVM decoders with a linear kernel for
944 population decoding[70]. For each mouse, we utilized the neural activity data collected
945 from 10 s before to 10 s after each trial, comparing it to resting state activity.
946 Decoders were trained on 80% of trials using a sliding 2-s time window and tested for
947 accuracy on the withheld 20% of trials. To avoid bias and overfitting, we repeated
948 decoding 512 times with random trial selections and averaged the measured values.

949 In tests examining the relationship between decoding accuracy and the number of
950 neurons, we randomly sampled increments of 200 (5%) neurons from a range of 200
951 to 4,000 neurons for decoding tests. The average decoding accuracy over the 15 s
952 duration of the air puff stimulus was recorded as the decoding accuracy for each
953 group of neurons. Each mouse underwent this random sampling 10 times to mitigate
954 the random errors caused by uneven distribution of neurons across brain regions.

955 **Global Neural Peak Activity Conduction Bar Graph**

956 In each trial, we observed specific directional inter-regional transmission of
957 neural group signals. To visualize fluctuations, we divided the AP = [-3 mm, 3 mm]
958 area into 16 bins and categorized the neurons within each. Since calcium signaling
959 serves as a low-pass, non-linear proxy for the sequence of cellular action potentials
960 (spikes), and the spike probabilities inferred by the cascade algorithm can be
961 considered a Gaussian kernel convolution of the spike sequence, generally featuring a
962 relatively higher temporal resolution, we averaged the spike probabilities S ($N_b \times N_t$,
963 where N_b is the number of regional bins and N_t is the number of time points) across
964 all neurons in each bin to obtain S_{bin}. This was then normalized to the peak values
965 within a 2 s window before and after each stimulation to generate the peak
966 transmission matrix T:

967 $$T = S_{bin} / Speak \quad (18)$$

968 Subsequently, we generated a 3D visualization of matrix T, showing normalized
969 signal fluctuations across regions and the sequence and timing of peak arrivals in
970 response to a single stimulus (Fig. 4J and Extended Data Fig. 5H,I).

971 **Dimensional Reduction and Visualization of Neural Representations Using**
972 **CEBRA**

To investigate whether global network-wide reorganization of activity patterns occurs during adaptation to repeated sensory stimuli, we employed the CEBRA[71] algorithm for dimensional reduction and visualization of neural representations. For our study, the CEBRA algorithm was applied to neuron signals that vary over time, specifically in the CEBRA-Time mode. The input consisted of spike probabilities from neurons across 10 trials. During the application of the CEBRA algorithm, we employed a nonlinear convolutional neural network model, the "offset10-model," for self-supervised training. The batch size for training data was set at 512, with a learning rate of 0.0003 for the optimizer, and a maximum iteration count of 10,000. The multi-dimensional neural signals were reduced to a three-dimensional space, with both the training and testing phases accelerated by high-performance graphics processing units. To enhance the visualization of the dimensional reduction results, we employed pseudocolor coding that changes over time to represent each time point in the reduced data, as shown in Fig. 4K.

Canonical Correlation Analysis and Principal Component Analysis of Pattern Shifts and Neural Activity Weight Changes

To investigate the correlation between activity patterns across different cortical areas and their gradual representational changes over successive experiments, we employed Canonical Correlation Analysis (CCA) to analyze the shifts in shared activity patterns within pairs of experiments and brain regions. For each experiment, the spike probability was captured within a 1.5 s window before and after stimulus presentation, segregated by brain region. For a given pair of trials within a specific brain region, we represented the dynamical features of this area during the two trials with matrices X and Y, sized $N_{t1} \times N_1$ and $N_{t2} \times N_2$, respectively. Here, N_{t1} and N_{t2} denote the total number of time points in the group dynamic matrices for the two trials, while N_1 and N_2 represent the number of neurons in each trial. Following the standard methodology of CCA, we identified two sets of loading vectors, $\{\boldsymbol{w}_i\}$ and $\{\boldsymbol{v}_i\}$. Each vector represents the weight distribution of each neural ensemble in a shared activity pattern observed across the two trials. The index i, ranging from 1 to the minimum of the dimensions of X and Y, denotes each mode. We determined these

1003 modes such that the projections of the neural activity fluctuations, X and Y onto $\boldsymbol{w}_i$
1004 and $\boldsymbol{v}_i$, achieved maximum correlation between the two ensembles.

1005 The maximization of the correlation between these projections is expressed as:

1006 $$\text{Maximize}_{\boldsymbol{w}_i,\boldsymbol{v}_i}(\mathrm{X}\boldsymbol{w}_i)^{\mathrm{T}}(\mathrm{Y}\boldsymbol{v}_i) \tag{19}$$

1007 subject to the normalization constraint: $\boldsymbol{w}_i^{\mathrm{T}}\mathrm{X}^{\mathrm{T}}\mathrm{X}\boldsymbol{w}_i = \boldsymbol{v}_i^{\mathrm{T}}\mathrm{Y}^{\mathrm{T}}\mathrm{Y}\boldsymbol{v}_i = 1$. Given this
1008 normalization condition, the quantity $(\mathrm{X}\boldsymbol{w}_i)^{\mathrm{T}} \cdot (\mathrm{Y}\boldsymbol{v}_i)$ equals the correlation
1009 coefficient r_i of the activity modes, $\mathrm{X}\boldsymbol{w}_i$ and $\mathrm{Y}\boldsymbol{v}_i$, in the two different trials.

1010 In order to explore the origins of gradual shifts in global activity patterns in
1011 response to stimuli and the involvement of different brain regions in these changes,
1012 we initially normalized the correlation coefficient r_1 for mode 1 extracted between
1013 different trials for each brain region, and visualized this data using a correlation
1014 heatmap (Fig. 4M). Subsequently, for each trial, we conducted cross-CCA between
1015 brain regions. Specifically, within a given independent trial, we performed cross-CCA
1016 on the dynamic matrices of the M, S, V, and RSP regions sequentially, obtaining
1017 pairwise correlated modes w_{areaij} and v_{areaij}. These modes were then averaged
1018 according to brain region:

1019 $$w_{\mathrm{area}i_{\mathrm{global}}} = \frac{\sum_j w_{\mathrm{area}ij_{\mathrm{global}}}}{N_{\mathrm{area}}} \tag{20}$$

1020 this calculation yielded a single-trial local loading vector $w_{\mathrm{area}i_{\mathrm{global}}}$ for each brain
1021 region, where N_{area} denotes the number of brain regions. Here, $w_{\mathrm{area}i_{\mathrm{global}}}$ reflects
1022 the absolute contribution of all neurons in that region to the global activity pattern
1023 during that trial. We posited that as trials progressed, the variation in these patterns
1024 would manifest in slow changes in the weight distribution of neuronal responses
1025 across different regions (Extended Data Fig. 5M). Accordingly, we mapped the
1026 changes in neuronal contribution weights $\boldsymbol{w}_{\mathrm{weight}_{\mathrm{change}}}$ across trials for different brain
1027 regions using the weight change matrix:

1028 $$w_{\mathrm{weight}_{\mathrm{change}}} = \left[w_{\mathrm{area1}_{\mathrm{global}}}, w_{\mathrm{area2}_{\mathrm{global}}}, \ldots w_{\mathrm{area10}_{\mathrm{global}}}\right] \tag{21}$$

1029 these changes were visualized (Extended Data Fig. 4M) and further analyzed using

PCA to reduce the dimensions of the weight change matrix. The dominant latent component, PC1 (Extended Data Fig. 5L), revealed gradual shifts in the contribution weights of neurons across different brain regions.

Additionally, we focused on the collective contributions of each brain region to the global activity pattern across ten trials. We projected the group activity of different regions onto the global activity pattern and averaged it across neurons, i.e.,

$$\text{Projection signal} = \text{mean}\left(\mathrm{X}w_{\text{area}i_{\text{global}}} \cdot w_{\text{area}i_{\text{global}}}\mathrm{T}\right) \tag{22}$$

It was observed that, despite all regions participating in the encoding response to air-puff stimuli and undergoing similar changes in neuronal contribution weights through successive adaptations, the activity patterns in regions S and V contributed more significantly to global encoding compared to regions M and RSP (Fig. 4L and Extended Data Fig. 5K).

Dissecting layer 2/3 and layer 5 activity simultaneously across cortex during anesthesia

Experiment Paradigm

A facemask was positioned in front of head-fixed *Camk2α-Cre::fl-GCaMP6s* mice and adjusted to fit snugly (gas flow 1.0 L/min). After a 30-min adaptation, 10-min awake baseline imaging was performed. Isoflurane was then increased to 2% for 20-min anesthesia induction, followed by a 10-min stabilization. Isoflurane was reduced to 0% for the recovery imaging. Simultaneous dual-layer imaging at 300-μm and 560-μm depth (6,000 × 6,000 μm^2 FOV) used the parabolic lateral collection module at 2,048 × 2,048-pixels resolution (7.67 Hz) .

Analysis of Synchrony in Neuronal Population Activity

To investigate changes in synchrony between deep and shallow neuronal activity during various stages of isoflurane anesthesia, we computed the Pearson correlation coefficient, R, for individual neurons against the remaining population activity within each window. This was performed using a 15 s time window with a 3 s step size:

$$R = \frac{E[(x-\mu_x)(y-\mu_y)]}{\sigma_x \sigma_y} \tag{23}$$

where x represents the activity of a single neuron within the window, y represents the activity of the excluded neuronal population and μ_x, μ_y denote the means of x and y, respectively, while σ_x and σ_y represent their standard deviations. E signifies the arithmetic mean. The mean correlation across all neurons was then used to quantify the synchrony of population activity within that window (Fig. 5F,G). Subsequently, we defined the probability of anesthesia-related events based on synchrony, using a 650 ms time window. Specifically, the peak synchrony during wakefulness and the lowest synchrony during anesthesia were used as thresholds to calculate the probability of population activity synchrony crossing these thresholds across multiple experiments.

To compare the synchrony differences between deep and shallow layers under different anesthetic states, we also analyzed the synchrony within the first 180 s following the onset of synchronized activity, typically between 40 s and 220 s after administration and cessation of isoflurane. Both during the induction and the awakening phases, neurons in both layers exhibited synchronized activity, with deeper layers showing higher synchrony than shallow layers, and induction phases showing higher synchrony than anesthesia phases (Fig. 5H, $p < 0.001$; Tukey test; neurons = 19,808 ~ 23,684; n = 3 mice).

Granger Causality Analysis

Based on experimental observations, we hypothesized that multiple "synchronized activities" during the induction of anesthesia actually represent specific directional flows rather than complete synchrony. To infer causality in activity between anterior and posterior (AP) cortical regions during individual synchronized events (synchronization peaks), we uniformly divided the cortical populations within an AP range of [-3 mm, 3 mm] into 16 segments. We then analyzed Granger causality among these 16 groups of neurons using the MVGC Multivariate Granger Causality Toolbox (https://github.com/lcbarnett/MVGC1)[72]. The input matrix included three dimensions: AP bins, time points, and peaks number, recording activity of different AP bins' neuronal populations within a 4 s interval (2 s before to 2 s after each peak).

1087 This multivariate Granger causality toolkit, based on a vector autoregressive model,
1088 calculates Granger causality where the model order (time lags) was estimated by
1089 Akaike Information Criteria with the maximum set to 20. Pairwise conditional
1090 causality was then calculated, where causality includes directional information: the
1091 direction "from" an X module "to" a Y module indicates that activity in X preceded
1092 that in Y. Granger causality values that reached $p < 0.05$ (Granger F test) after
1093 applying the false discovery rate for multiple-comparison correction (Fig. 5I).

1094 **Analysis of Global Neural Activity Transmission During Synchronous Peaks**

1095 During periods of anesthesia, multiple "synchronous" peaks are not entirely
1096 synchronized and exhibit various directions of transmission. It is only during deep
1097 anesthesia that these "synchronous" peaks approach complete synchronization. To
1098 verify this, similar to the repetitive air-puff whisker stimulation experiment, we
1099 initially utilized the spike probability outputs from NeuroPixelAI to perform regional
1100 peak detection, resulting in the generation of a spike transmission matrix $\mathrm{T}_{\mathrm{peaks}}$. Here,
1101 peak detection was conducted using a MATLAB-based local thresholding algorithm,
1102 with parameters set at a threshold of 0.001, minimum peak height of 0.04, and
1103 minimum peak distance of 20. The structure of $\mathrm{T}_{\mathrm{peaks}}$ is represented as $N_{\mathrm{b}} \cdot N_{\mathrm{t}} \cdot$
1104 $\mathrm{peaks}_{\mathrm{num}}$, where N_{b} denotes the number of regional bins, N_{t} indicates the number
1105 of time points (spanning [-2 s, 2 s] across 31 frames at a frame rate of 7.67), and
1106 $\mathrm{peaks}_{\mathrm{num}}$ represents the detected number of peaks. A three-dimensional visualization
1107 of the signals within $\mathrm{T}_{\mathrm{peaks}}$ facilitates the generation of a global map of neural peak
1108 activity transmission (Fig. 5J and Extended Data Fig. 6C).

1109 To further visualize the dynamic transmission process of "synchronous" signals
1110 throughout the anesthesia induction, we rendered a global dynamic transmission map
1111 of peak activities at the resolution of individual neurons (Fig. 5J, Extended Data Fig.
1112 6A,C, and Supplementary Video). In this representation, yellow signifies the origin
1113 regions of the signals, while purple denotes the receiving regions. Specifically, for
1114 each "synchronous" event, we normalized the spike probability for each neuron
1115 around the event ([-2 s, 2 s]), based on peak values. We then calculated the response

delay, which is the difference between the peak positions of individual neurons and the peak position of the group activity. If the response delay is less than zero, the neuron is identified as the source of the event; if greater than zero, the neuron is considered a receiver. Based on the response delays of various neurons, we were able to ascertain the global dynamics of peak transmission within the imaging field area (6,000 × 6,000 μm^2): for each layer in T_{peaks}, or each peak, we determined the times t_{AP} at which different AP bins reached their peak and calculated the standard deviation across these bins:

$$\text{Global response delay} = \sqrt{\frac{\sum_i (t_{AP,i} - \bar{t}_{AP,i})^2}{N_b - 1}} \tag{24}$$

the global response delay reflects the fluidity of each spike's global response, illustrating the progression from incomplete to almost complete synchronization of multiple "synchronous" peaks during the entire period of anesthesia induction (Extended Data Fig. 6B). To mitigate the impact of spurious spikes detected during peak detection, we applied a sliding window averaging and normalization over 20 spikes.

Through the assessment of global response delays, we hypothesize that during the process of anesthesia induction, there exists a gradual change in neural group activities and a redistribution of neuronal activity weights, associated with an increase in 'synchronized' peak events. To investigate this, we categorized the detected peaks into deciles, representing 10% of the peaks per group, and initially computed the normalized CCA mode1 correlation matrices between these groups (Fig. 5L). Subsequently, we demonstrated the matrices of changes in neuronal weight across these ten groups of peaks (Extended Data Fig. 6D). The correlation coefficient matrices were derived through pairwise CCA of each group of peaks. The CCA of the neuronal weight change matrices encompassed two elements: the neural dynamics matrix for the period [-2s, 2s] around a specific group of peaks, and the average neural dynamics matrix for all other peaks except for the group in question. Following each CCA, the weight matrices w_i were normalized (ensuring the sum of weights for all neurons equaled one) and subjected to iterative correlation ranking.

1145 In addition, we analyzed the proportions of forward versus backward
1146 transmission peaks (Fig. 5L; $p < 0.05$) and the transmission from deep to shallow
1147 layers versus from shallow to deep layers during the entire anesthesia induction
1148 process (Extended Data Fig. 6F; $p < 0.01$). For the anterior-posterior peak
1149 transmission, we calculated the difference in response delays between the first 50% of
1150 bins and the last 50% of each event to determine whether the anterior or posterior
1151 regions reached peak values first. For the deep-to-shallow layer transmission, we
1152 calculated the differences in response delays across 16 bins corresponding to different
1153 depths(Extended Data Fig. 6E). A negative response delay indicated that, for a given
1154 event, the signal was transmitted from deeper to more shallow layers; conversely, a
1155 positive response delay suggested transmission from shallow to deeper layers. These
1156 findings align with previous studies[73-76], indicating that during the anesthesia induction
1157 phase, global signal propagation predominantly occurs from posterior to anterior
1158 regions, with notable instances of reverse transmission, primarily occurring from
1159 deeper to more shallow layers.

1160 Dynamic monitoring of MNP distribution and vascular occlusion in 1161 the living brain

1162 Experiment Paradigm

1163 Prior to imaging, male *C57BL/J* mice (Charles River Laboratories #219) under
1164 isoflurane anesthetized received 200-μL retro-orbital injections of 5% FITC-Dextran
1165 or RITC-Dextran. Twenty-eight-layer structural vascular imaging at 450-μm depth
1166 cover 6,000 × 6,000 × 450 μm^3 (4× objective) or 1600 × 1600 × 450 μm^3 volumes
1167 (16× objective), using the parabolic lateral module at 2,048 × 2,048 pixels resolution
1168 (7.67 Hz/layer). For real-time MNPs tracking, dye-injected mice received 100-μL tail
1169 vein injections of 1 mg/mL 5-μm polystyrene (PS) microplastics (MPs, BEISILE
1170 #7-1-0500) or 200-nm PS nanoplastics (NPs, BEISILE #7-3-0020) during single-layer
1171 imaging. Repeat 28-layer structural imaging was performed at 12-h and 24-h
1172 post-injection.

1173 Blood Flow Velocity Detection

1174 Blood flow velocity was measured using an established method[77]. Fluorescent
1175 dye injection rendered red blood cells (RBCs) as dark particles. RBC displacement
1176 was tracked by 1k Hz high-speed line-scanning within ROIs. Velocity was calculated
1177 from pixel-wise displacement over 10-s line-scanning recordings. Given MNP
1178 occlusion-prone capillaries, we analyzed single-RBC-perfused vessels. Measurements
1179 occurred at: 1-h post-anesthesia (avoiding stress hyperemia), and 12/24-h
1180 post-injection. Blood flow was not assessed during tail vein injections to eliminate
1181 artifacts.

1182 **Blood-Brain Barrier Integrity Assay**

1183 Male *C57BL/J* mice were divided into: sham-operated, 5-day post-surgery, and
1184 14-day post-surgery groups. Each received 125-μL tail vein injections of 2% Evans
1185 Blue (Beyotime Biotechnology #ST3273) 1.5 h before brain collection. Mice were
1186 anesthetized with 1% pentobarbital sodium (i.p.), then transcardially perfused with
1187 heparinized saline (20 U/mL) and 4% PFA. Evans Blue extravasation was visually
1188 assessed in whole brains to qualitatively evaluate BBB integrity.

1189 # References

1190 1. Li, K., Nakajima, M., Ibañez-Tallon, I. & Heintz, N. A Cortical Circuit for Sexually
1191 Dimorphic Oxytocin-Dependent Anxiety Behaviors. *Cell* **167**, 60-72.e11 (2016).
1192 2. Buzsáki, G. & Draguhn, A. Neuronal Oscillations in Cortical Networks. *Science* **304**,
1193 1926-1929 (2004).
1194 3. Vyas, S., Golub, M.D., Sussillo, D. & Shenoy, K.V. Computation Through Neural Population
1195 Dynamics. *Annual Review of Neuroscience* **43**, 249-275 (2020).
1196 4. Kim, T.H. & Schnitzer, M.J. Fluorescence imaging of large-scale neural ensemble dynamics.
1197 *Cell* **185**, 9-41 (2022).
1198 5. Denk, W., Strickler, J.H. & Webb, W.W. Two-Photon Laser Scanning Fluorescence
1199 Microscopy. *Science* **248**, 73-76 (1990).
1200 6. Helmchen, F. & Denk, W. Deep tissue two-photon microscopy. *Nature Methods* **2**, 932-940
1201 (2005).
1202 7. Cahalan, M.D., Parker, I., Wei, S.H. & Miller, M.J. Two-photon tissue imaging: seeing the
1203 immune system in a fresh light. *Nature Reviews Immunology* **2**, 872-880 (2002).
1204 8. Wu, J., Ji, N. & Tsia, K.K. Speed scaling in multiphoton fluorescence microscopy. *Nature*
1205 *Photonics* **15**, 800-812 (2021).
1206 9. Hampson, K.M. et al. Adaptive optics for high-resolution imaging. *Nature Reviews Methods*
1207 *Primers* **1**, 68 (2021).
1208 10. Pittet, Mikael J. & Weissleder, R. Intravital Imaging. *Cell* **147**, 983-991 (2011).

1209 11. Ji, N., Magee, J.C. & Betzig, E. High-speed, low-photodamage nonlinear imaging using
1210 passive pulse splitters. *Nature Methods* **5**, 197-202 (2008).
1211 12. Zipfel, W.R., Williams, R.M. & Webb, W.W. Nonlinear magic: multiphoton microscopy in the
1212 biosciences. *Nature Biotechnology* **21**, 1369-1377 (2003).
1213 13. Stirman, J.N., Smith, I.T., Kudenov, M.W. & Smith, S.L. Wide field-of-view, multi-region,
1214 two-photon imaging of neuronal activity in the mammalian brain. *Nature Biotechnology* **34**,
1215 857-862 (2016).
1216 14. Tsai, P.S. et al. Ultra-large field-of-view two-photon microscopy. *Opt. Express* **23**,
1217 13833-13847 (2015).
1218 15. Ota, K. et al. Fast, cell-resolution, contiguous-wide two-photon imaging to reveal functional
1219 network architectures across multi-modal cortical areas. *Neuron* **109**, 1810-1824.e1819
1220 (2021).
1221 16. Clough, M. et al. Flexible simultaneous mesoscale two-photon imaging of neural activity at
1222 high speeds. *Nature Communications* **12**, 6638 (2021).
1223 17. Zhang, Y. et al. Long-term mesoscale imaging of 3D intercellular dynamics across a
1224 mammalian organ. *Cell* **187**, 6104-6122.e6125 (2024).
1225 18. Mengke, Y. et al. Ultra-wide-field, deep, adaptive two-photon microscopy. *bioRxiv -*
1226 *Neuroscience* (2025).
1227 19. Yu, C.-H. et al. The Cousa objective: a long-working distance air objective for multiphoton
1228 imaging in vivo. *Nature Methods* **21**, 132-141 (2024).
1229 20. Yu, C.-H., Stirman, J.N., Yu, Y., Hira, R. & Smith, S.L. Diesel2p mesoscope with dual
1230 independent scan engines for flexible capture of dynamics in distributed neural circuitry.
1231 *Nature Communications* **12**, 6639 (2021).
1232 21. Mok, A.T. et al. A large field-of-view, single-cell-resolution two- and three-photon microscope
1233 for deep and wide imaging. *eLight* **4**, 20 (2024).
1234 22. Rumyantsev, O.I. et al. Fundamental bounds on the fidelity of sensory cortical coding. *Nature*
1235 **580**, 100-105 (2020).
1236 23. Sofroniew, N.J., Flickinger, D., King, J. & Svoboda, K. A large field of view two-photon
1237 mesoscope with subcellular resolution for in vivo imaging. *eLife* **5**, e14472 (2016).
1238 24. Lu, R. et al. Rapid mesoscale volumetric imaging of neural activity with synaptic resolution.
1239 *Nature Methods* **17**, 291-294 (2020).
1240 25. Demas, J. et al. High-speed, cortex-wide volumetric recording of neuroactivity at cellular
1241 resolution using light beads microscopy. *Nature Methods* **18**, 1103-1111 (2021).
1242 26. Pachitariu, M. et al. Suite2p: beyond 10,000 neurons with standard two-photon microscopy.
1243 *bioRxiv*, 061507 (2017).
1244 27. Giovannucci, A. et al. CaImAn an open source tool for scalable calcium imaging data analysis.
1245 *eLife* **8**, e38173 (2019).
1246 28. Lu, J. et al. MIN1PIPE: A Miniscope 1-Photon-Based Calcium Imaging Signal Extraction
1247 Pipeline. *Cell Reports* **23**, 3673-3684 (2018).
1248 29. Li, X. et al. Real-time denoising enables high-sensitivity fluorescence time-lapse imaging
1249 beyond the shot-noise limit. *Nature Biotechnology* **41**, 282-292 (2023).
1250 30. Li, X. et al. Spatial redundancy transformer for self-supervised fluorescence image denoising.
1251 *Nature Computational Science* **3**, 1067-1080 (2023).

1252 31. Chen, T.-W. et al. Ultrasensitive fluorescent proteins for imaging neuronal activity. *Nature* **499**,
1253 295-300 (2013).
1254 32. Akerboom, J. et al. Optimization of a GCaMP Calcium Indicator for Neural Activity Imaging.
1255 *The Journal of Neuroscience* **32**, 13819 (2012).
1256 33. Faisal, A.A., Selen, L.P.J. & Wolpert, D.M. Noise in the nervous system. *Nature Reviews*
1257 *Neuroscience* **9**, 292-303 (2008).
1258 34. Lütcke, H., Margolis, D.J. & Helmchen, F. Steady or changing? Long-term monitoring of
1259 neuronal population activity. *Trends in Neurosciences* **36**, 375-384 (2013).
1260 35. Stein, R.B., Gossen, E.R. & Jones, K.E. Neuronal variability: noise or part of the signal?
1261 *Nature Reviews Neuroscience* **6**, 389-397 (2005).
1262 36. Zohary, E., Shadlen, M.N. & Newsome, W.T. Correlated neuronal discharge rate and its
1263 implications for psychophysical performance. *Nature* **370**, 140-143 (1994).
1264 37. Driscoll, L.N., Pettit, N.L., Minderer, M., Chettih, S.N. & Harvey, C.D. Dynamic
1265 Reorganization of Neuronal Activity Patterns in Parietal Cortex. *Cell* **170**, 986-999.e916
1266 (2017).
1267 38. Montijn, Jorrit S., Meijer, Guido T., Lansink, Carien S. & Pennartz, Cyriel M.A.
1268 Population-Level Neural Codes Are Robust to Single-Neuron Variability from a
1269 Multidimensional Coding Perspective. *Cell Reports* **16**, 2486-2498 (2016).
1270 39. Ebrahimi, S. et al. Emergent reliability in sensory cortical coding and inter-area
1271 communication. *Nature* **605**, 713-721 (2022).
1272 40. Dong, Y., Li, J., Zhou, M., Du, Y. & Liu, D. Cortical regulation of two-stage rapid eye
1273 movement sleep. *Nature Neuroscience* **25**, 1675-1682 (2022).
1274 41. Brown, R., Lau, H. & LeDoux, J.E. Understanding the Higher-Order Approach to
1275 Consciousness. *Trends in Cognitive Sciences* **23**, 754-768 (2019).
1276 42. Franco, S.J. et al. Fate-Restricted Neural Progenitors in the Mammalian Cerebral Cortex.
1277 *Science* **337**, 746-749 (2012).
1278 43. Mashour, G.A., Roelfsema, P., Changeux, J.-P. & Dehaene, S. Conscious Processing and the
1279 Global Neuronal Workspace Hypothesis. *Neuron* **105**, 776-798 (2020).
1280 44. Muindi, F. et al. Electrical stimulation of the parabrachial nucleus induces reanimation from
1281 isoflurane general anesthesia. *Behavioural Brain Research* **306**, 20-25 (2016).
1282 45. Bharioke, A. et al. General anesthesia globally synchronizes activity selectively in layer 5
1283 cortical pyramidal neurons. *Neuron* **110**, 2024-2040.e2010 (2022).
1284 46. Steriade, M., Nuñez, A. & Amzica, F. A novel slow (<1 Hz) oscillation of neocortical neurons
1285 in vivo: Depolarizing and hyperpolarizing components. *The Journal of Neuroscience* **13**,
1286 3252-3265 (1993).
1287 47. Pal, D. et al. Differential Role of Prefrontal and Parietal Cortices in Controlling Level of
1288 Consciousness. *Current Biology* **28**, 2145-2152.e2145 (2018).
1289 48. Gao, S., Proekt, A., Renier, N., Calderon, D.P. & Pfaff, D.W. Activating an anterior nucleus
1290 gigantocellularis subpopulation triggers emergence from pharmacologically-induced coma in
1291 rodents. *Nature Communications* **10**, 2897 (2019).
1292 49. Nihart, A.J. et al. Bioaccumulation of microplastics in decedent human brains. *Nature*
1293 *Medicine* **31**, 1114-1119 (2025).
1294 50. Thompson, R.C. et al. Twenty years of microplastic pollution research—what have we learned?
1295 *Science* **386**, eadl2746 (2024).

51. Song, A., Gauthier, J.L., Pillow, J.W., Tank, D.W. & Charles, A.S. Neural anatomy and optical microscopy (NAOMi) simulation for evaluating calcium imaging methods. *Journal of Neuroscience Methods* **358**, 109173 (2021).
52. Meiniel, W., Olivo-Marin, J.C. & Angelini, E.D. Denoising of Microscopy Images: A Review of the State-of-the-Art, and a New Sparsity-Based Method. *IEEE Transactions on Image Processing* **27**, 3842-3856 (2018).
53. Li, X. et al. Reinforcing neuron extraction and spike inference in calcium imaging using deep self-supervised denoising. *Nature Methods* **18**, 1395-1400 (2021).
54. Rupprecht, P. et al. A database and deep learning toolbox for noise-optimized, generalized spike inference from calcium imaging. *Nature Neuroscience* **24**, 1324-1337 (2021).
55. Pachitariu, M. & Stringer, C. Cellpose 2.0: how to train your own model. *Nature Methods* **19**, 1634-1641 (2022).
56. Pnevmatikakis, Eftychios A. et al. Simultaneous Denoising, Deconvolution, and Demixing of Calcium Imaging Data. *Neuron* **89**, 285-299 (2016).
57. Bao, Y., Soltanian-Zadeh, S., Farsiu, S. & Gong, Y. Segmentation of neurons from fluorescence calcium recordings beyond real time. *Nature Machine Intelligence* **3**, 590-600 (2021).
58. Rose, T., Goltstein, P.M., Portugues, R. & Griesbeck, O. Putting a finishing touch on GECIs. *Frontiers in Molecular Neuroscience* **Volume 7 - 2014** (2014).
59. Wei, Z. et al. A comparison of neuronal population dynamics measured with calcium imaging and electrophysiology. *PLOS Computational Biology* **16**, e1008198 (2020).
60. Farhan, A. & Alex, C.K. Interpreting in vivo calcium signals from neuronal cell bodies, axons, and dendrites: a review. *Neurophotonics* 7, 011402 (2019).
61. Yeh, P.-T. et al. Discrete photoentrainment of mammalian central clock is regulated by bi-stable dynamic network in the suprachiasmatic nucleus. *Nature Communications* **16**, 3331 (2025).
62. Guyoton, M. et al. Cortical circuits for cross-modal generalization. *Nature Communications* **16**, 4230 (2025).
63. Shao, L.-X. et al. Psilocybin's lasting action requires pyramidal cell types and 5-HT2A receptors. *Nature* **642**, 411-420 (2025).
64. Russell, L.E. et al. All-optical interrogation of neural circuits in behaving mice. *Nature Protocols* **17**, 1579-1620 (2022).
65. Koukouli, F. et al. Nicotine reverses hypofrontality in animal models of addiction and schizophrenia. *Nature Medicine* **23**, 347-354 (2017).
66. Deneux, T. et al. Accurate spike estimation from noisy calcium signals for ultrafast three-dimensional imaging of large neuronal populations in vivo. *Nature Communications* **7**, 12190 (2016).
67. Schneider, C.A., Rasband, W.S. & Eliceiri, K.W. NIH Image to ImageJ: 25 years of image analysis. *Nature Methods* **9**, 671-675 (2012).
68. Wolf, E. Electromagnetic Diffraction in Optical Systems. I. An Integral Representation of the Image Field. *Proceedings of the Royal Society of London. Series A, Mathematical and Physical Sciences* **253**, 349-357 (1959).
69. Lein, E.S. et al. Genome-wide atlas of gene expression in the adult mouse brain. *Nature* **445**, 168-176 (2007).

70. Bellafard, A., Namvar, G., Kao, J.C., Vaziri, A. & Golshani, P. Volatile working memory representations crystallize with practice. *Nature* **629**, 1109-1117 (2024).
71. Schneider, S., Lee, J.H. & Mathis, M.W. Learnable latent embeddings for joint behavioural and neural analysis. *Nature* **617**, 360-368 (2023).
72. Barnett, L. & Seth, A.K. The MVGC multivariate Granger causality toolbox: A new approach to Granger-causal inference. *Journal of Neuroscience Methods* **223**, 50-68 (2014).
73. Pullon, R.M., Yan, L., Sleigh, J.W. & Warnaby, C.E. Granger Causality of the Electroencephalogram Reveals Abrupt Global Loss of Cortical Information Flow during Propofol-induced Loss of Responsiveness. *Anesthesiology* **133** (2020).
74. Huo, J. et al. Orexin signalling in the nucleus accumbens promotes arousal from isoflurane anaesthesia and restores communication between the nucleus accumbens and frontal cortex. *British Journal of Anaesthesia* (2025).
75. Yin, M. et al. Synchronicity of pyramidal neurones in the neocortex dominates isoflurane-induced burst suppression in mice. *British Journal of Anaesthesia* **134**, 1122-1133 (2025).
76. Song, X.-J. & Hu, J.-J. Neurobiological basis of emergence from anesthesia. *Trends in Neurosciences* **47**, 355-366 (2024).
77. Kim, T.N. et al. Line-Scanning Particle Image Velocimetry: An Optical Approach for Quantifying a Wide Range of Blood Flow Speeds in Live Animals. *PLOS ONE* **7**, e38590 (2012).

Resource availability

Lead contact

Further information and requests for resources and reagents should be directed to and will be fulfilled by the lead contact, Bo Li (liboresearch@gmail.com).

Materials availability

This study did not generate new unique reagents.

Data and code availability

The codes generated during this study with example data are available at GitHub with the following link: https://github.com/Yourswear/Meso2P. NeuroPixelAI are available with the following link: https://github.com/Yourswear/NeuroPixelAI. The published article includes all data generated during this study and all the raw data is also available from the corresponding author upon request. Any additional information required to reanalyze the data reported in this paper is available from the lead contact upon request.

Acknowledgements

This work was supported by the Shanghai Municipal Education Commission (2024RGZNB03), Fudan University (FudanX24AI048, yg2023-04), the National Natural Science Foundation of China (T2222006), and the Science and Technology Commission of Shanghai Municipality (20JC1419500).

Author Contributions

Conceptualization: B.L.; methodology: B.L., J.H.H., S.P.L., C.Y.L., M.Z.; biological experiments: Y.F.Z., J.H.H, X.Y.G.; Zemax optical simulation: J.H.H., F.X.; investigation: J.H.H., Y.F.Z.; visualization: J.H.H., Y.F.Z., M.Z.; funding acquisition: B.L., Y.M., L.C.; project administration: B.L.; writing: B.L., J.H.H, Y.F.Z. Y.M., L.C., J.C.W.

Declaration of interests

The authors declare no competing interests.

Extended data

Extended Data Fig. 1 Modular design schematic and performance evaluation of Meso2P imaging, related to Figures 1 and 2 and Methods.

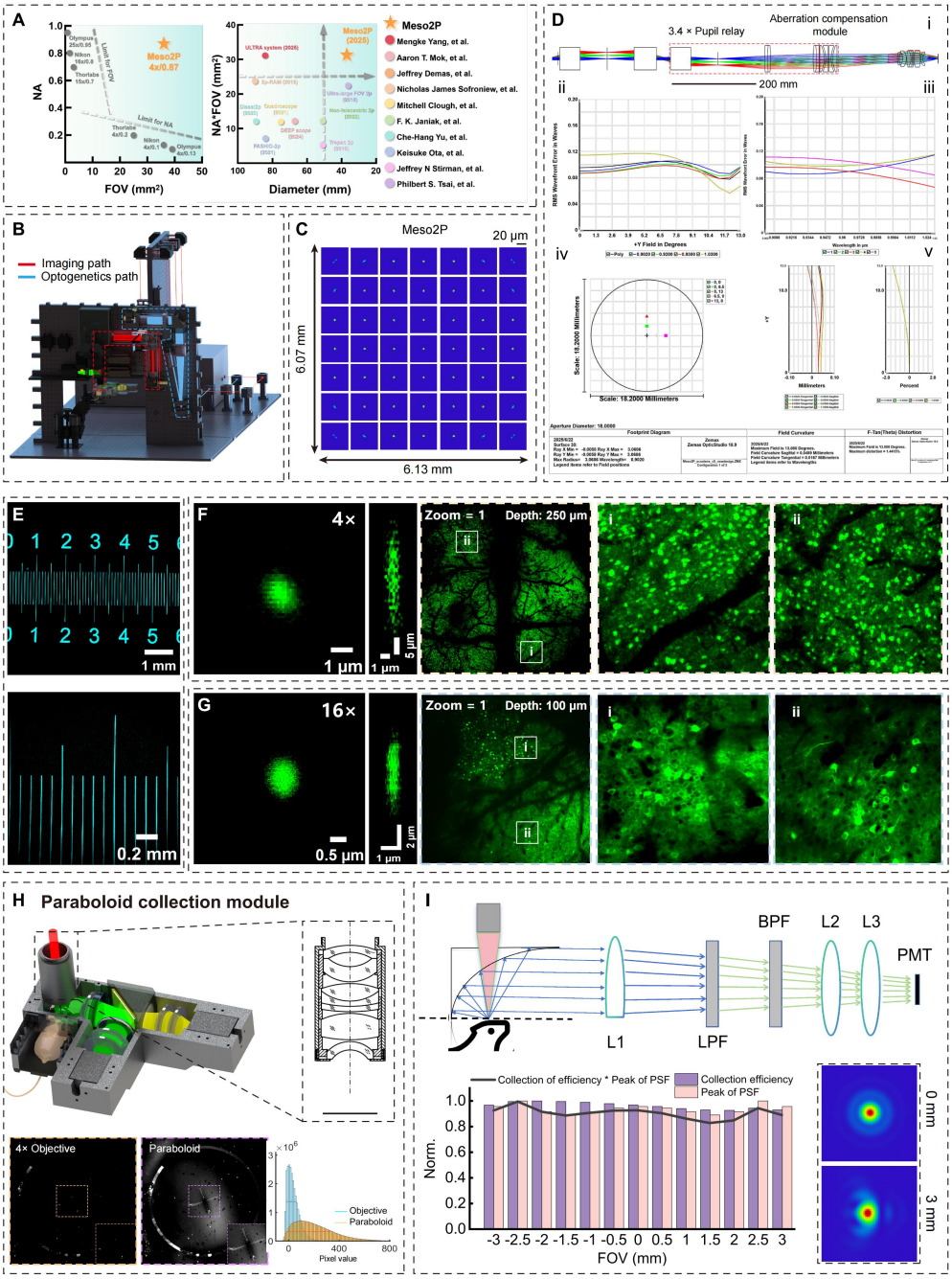

(A) Comparative analysis of Meso2P with other two-photon mesoscopes. Left, Meso2P overcomes traditional trade-offs between NA and FOV. Right, Meso2P demonstrates superior fluorescence collection efficiency and a smaller objective diameter compared to other mesoscopes. The NA and FOV were all derived from explicit or displayed parameters in the cited reference paper. **(B)** SolidWorks-rendered optical path geometry (excitation in blue, stimulation in orange). **(C)** Field-dependent aberration quantified by point spread function (PSF) profiles across the entire

FOV. **(D)** Optical simulation performance of Meso2P transverse scanning module. (i) Zemax optical path diagram. (ii) Field-dependent RMS wavefront aberration (0°: FOV center; 13°: 3 mm off-axis). (iii) Wavelength-dependent RMS wavefront aberration (blue: center; green: 1.5 mm off-axis; red: 3 mm off-axis). (iv) Spot diagram at focal plane demonstrating simulated 6.13 mm FOV. (v) Field curvature and distortion across entire FOV. **(E)** FOV calibration using fluorescent-etched scale bars. **(F)** Fundamental imaging characteristics of Meso2P with 4× objective. Left, example images of 0.1 μm fluorescent beads. Right, imaging demonstration with zoomed-in views of two regions (white boxes). **(G)** Same as (F), but for 16× objective. **(H)** Parabolic collection module: 3D model and imaging performance. Top, SolidWorks-rendered model (inset: custom 4× objective in dashed box). Bottom, Imaging comparison: objective-only vs. parabolic module collection (fluorescent-etched scale bar sample) with pixel intensity distribution. **(I)** Top, Optical principle of parabolic collection module. LPF, low-pass filter. BPF, band-pass filter. Bottom, field uniformity analysis (± 3 mm FOV): PSF peak intensities and collection efficiencies, with comparisons of PSF at the center and 3 mm edge.

Extended Data Fig. 2 Schematic implementation of diverse and flexible volumetric imaging using Meso2P, related to Figure 2 and Methods.

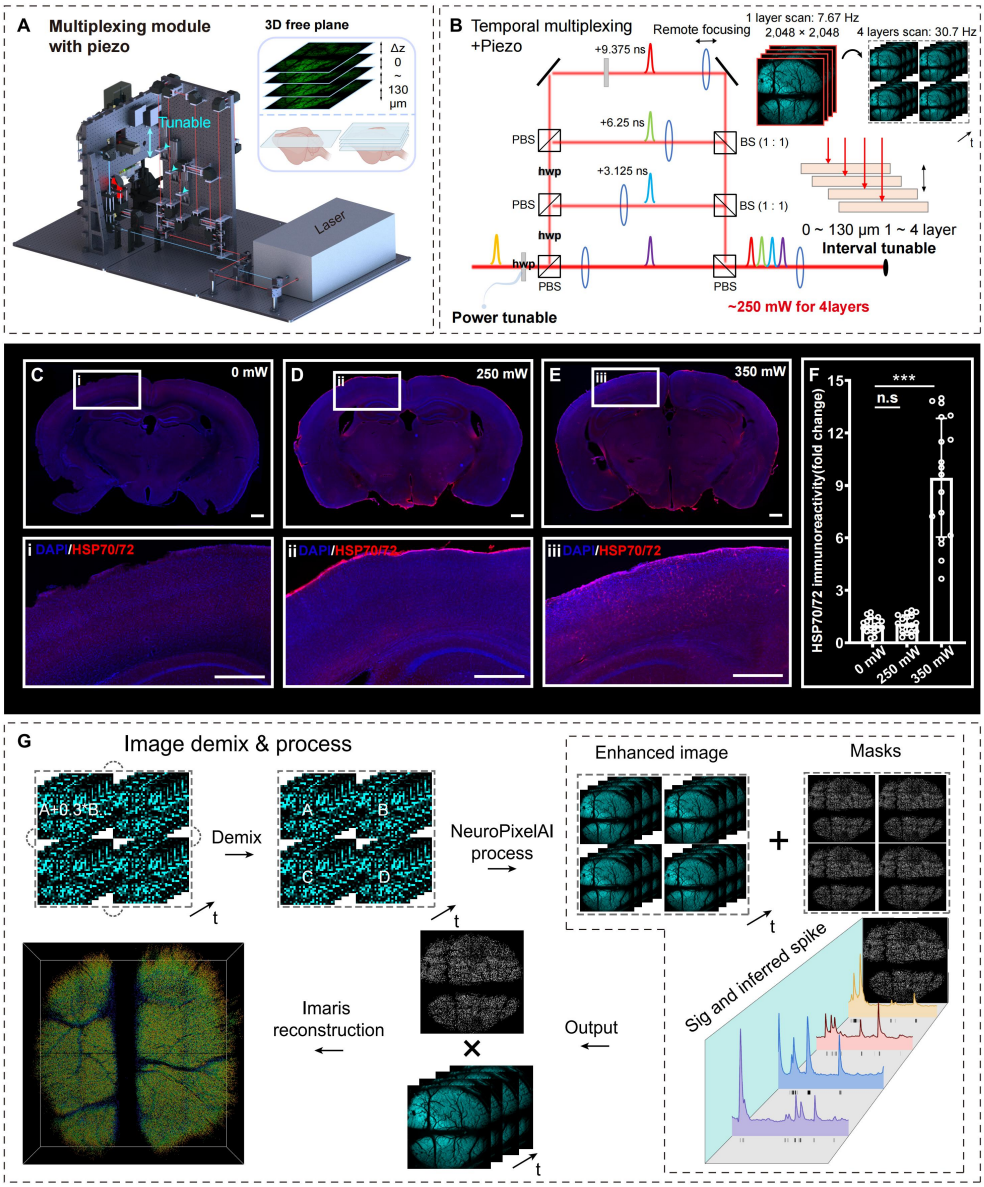

(A) 3D SolidWorks schematic of the dual-extension module for volumetric imaging. **(B)** Dual-extension module for volumetric imaging. BS: 50/50 beam splitter; PBS: polarizing beam splitter; HWP: rotatable half-wave plate. All lenses are mounted on programmable stages for focal adjustment. **(C-E)** Representative images of brain sections showing immunolabeling for thermal damage marker (anti-HSP70/72, red) and DNA stain (DAPI, blue) after exposure to the laser power listed below. (C) control, no laser exposure; (D) 250 mw; (E) 350 mw. Scale bars: 500 μm. **(F)** Intensity of immunolabeling corresponding to imaging area as a fraction compared to mean of control samples. (n = 3 mice per group, 6 cortical regions per brain). n.s, no significance; ***$p < 0.001$; Tukey test. **(G)** Data processing pipeline for large-volume 3D imaging on the basis of NeuroPixelAI. Key steps: Four-layer image crosstalk elimination, neuron information extraction via NeuroPixelAI, mask generation and volumetric reconstruction in Imaris.

Extended Data Fig. 3 Experimental validation of the Meso2P extension module, related to Figure 2

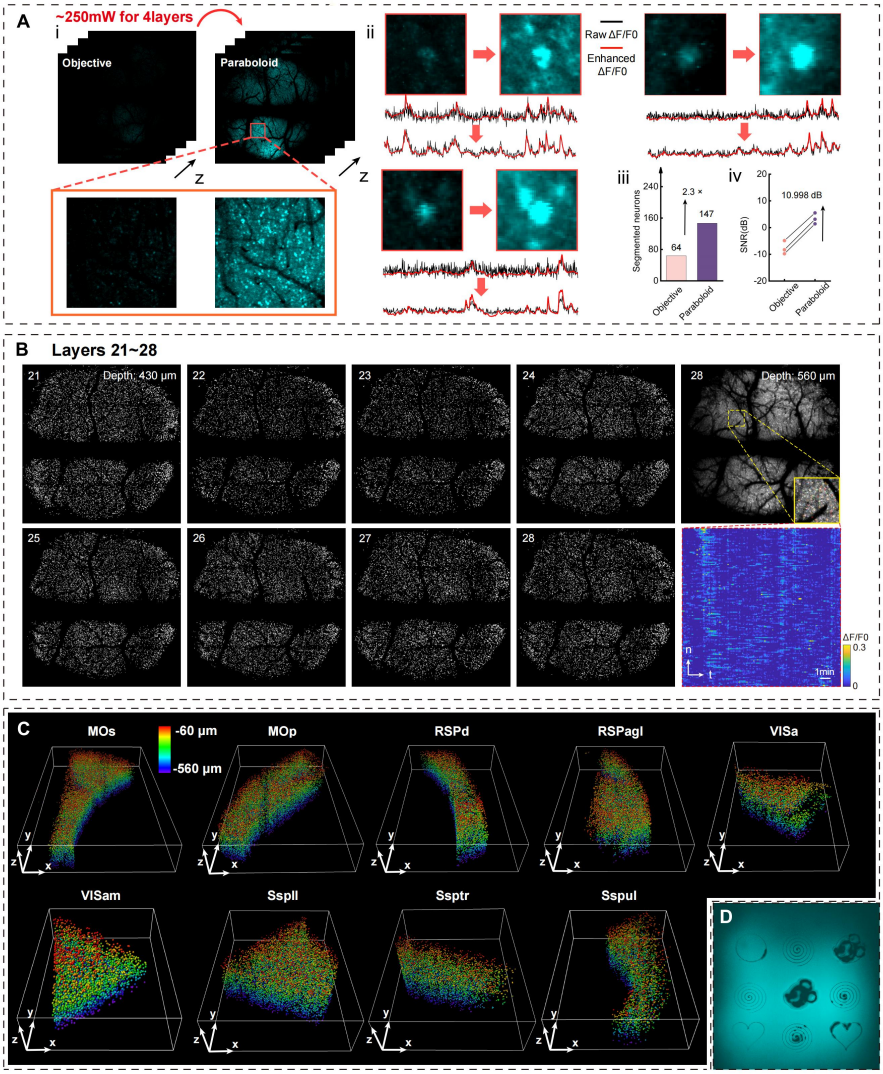

(A) Paraboloid collection module enhances neural imaging versus conventional objective. (i) Image quality comparison with a zoom-in region. (ii) Comparison of image quality and signal traces in single neurons (white arrows: example neurons; black/red traces, raw/NeuroPixelAI-enhanced signals). (iii) Segmentation improvement of neurons in (i). (iv) SNR enhancement of temporal signals from three marked neurons in (ii). **(B)** Example 3D segmentation masks across 28 imaging planes (layers 21-28; 430-560 μm below the surface). Right, example image at deepest layer (28) with zoomed-in neuronal regions (yellow boxes) and corresponding temporal signals. **(C)** 3D rendering of extracted neurons across nine representative brain regions (28 layers total). Neurons are colored by depth. **(D)** The representative holographic pattern presented by the galvo/SLM path.

Extended Data Fig. 4 Algorithm benchmarking and implementation schematics for NeuroPixelAI, related to Figure 3 and Methods.

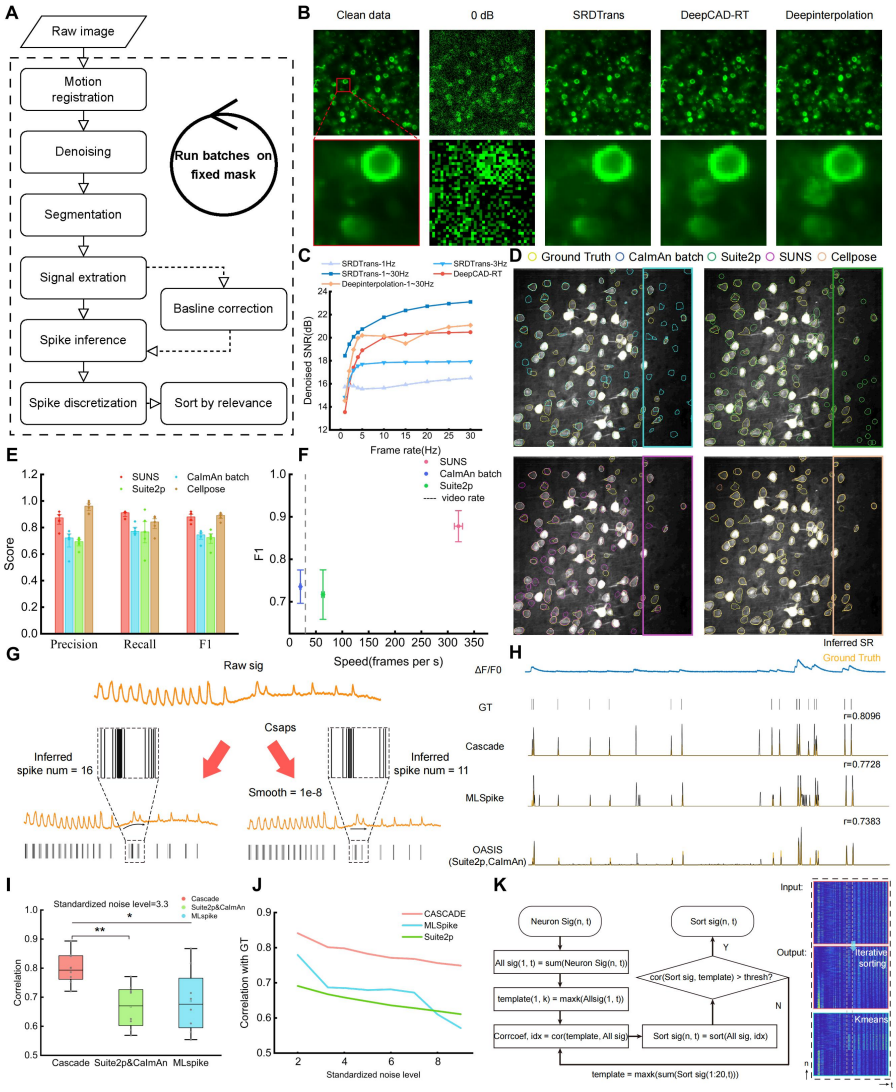

(A) Schematic workflow of the standard NeuroPixelAI processing pipeline. Key steps include motion registration, denoising, segmentation, signal extraction, baseline correction, spike inference, spike discretization, and iterative sorting. Batch processing of selected steps is enabled using predefined processing masks. **(B)** Performance comparison of denoising algorithms on noisy data (0 dB SNR). Bottom panels show zoomed-in views of example neurons. **(C)** Denoising algorithm performance across varying imaging frame rates (1–30 Hz). SRDTrans was trained on datasets at each specific frame rate; DeepCAD-RT utilized its published large pretrained model. **(D)** Comparison of segmentation algorithm performance. Boxed regions highlight areas exhibiting significant differences. **(E)** Bar plot showing F1 scores of segmentation algorithms. Data derived from two-photon and three-photon imaging at depths of 100–1000 μm (n = 5 mice). **(F)** Comparison of processing speed versus F1 score for segmentation algorithms. **(G)** Schematic and efficacy of baseline correction using a cubic spline interpolation algorithm. Correction (right) reduces erroneous spike inference caused by baseline drift. **(H)** Performance comparison of spike inference algorithms. Predicted spikes (black) versus ground truth (yellow). **(I)** Correlation

between inferred and ground-truth action potentials for spike inference algorithms across standardized noise levels. Datasets: Simultaneous electrophysiology and calcium imaging recordings from single neurons (GENIE datasets; n = 8 neurons). **(J)** Box plot statistics of inference correlation coefficients for all algorithms at a standardized noise level of 3.3. **(K)** Workflow and output of the label-free iterative sorting algorithm. Gray dashed lines indicate clear sorting results.

Extended Data Fig. 5 Large-scale population neural response dynamics during repetitive whisker stimulation, related to Figure 4 and Methods.

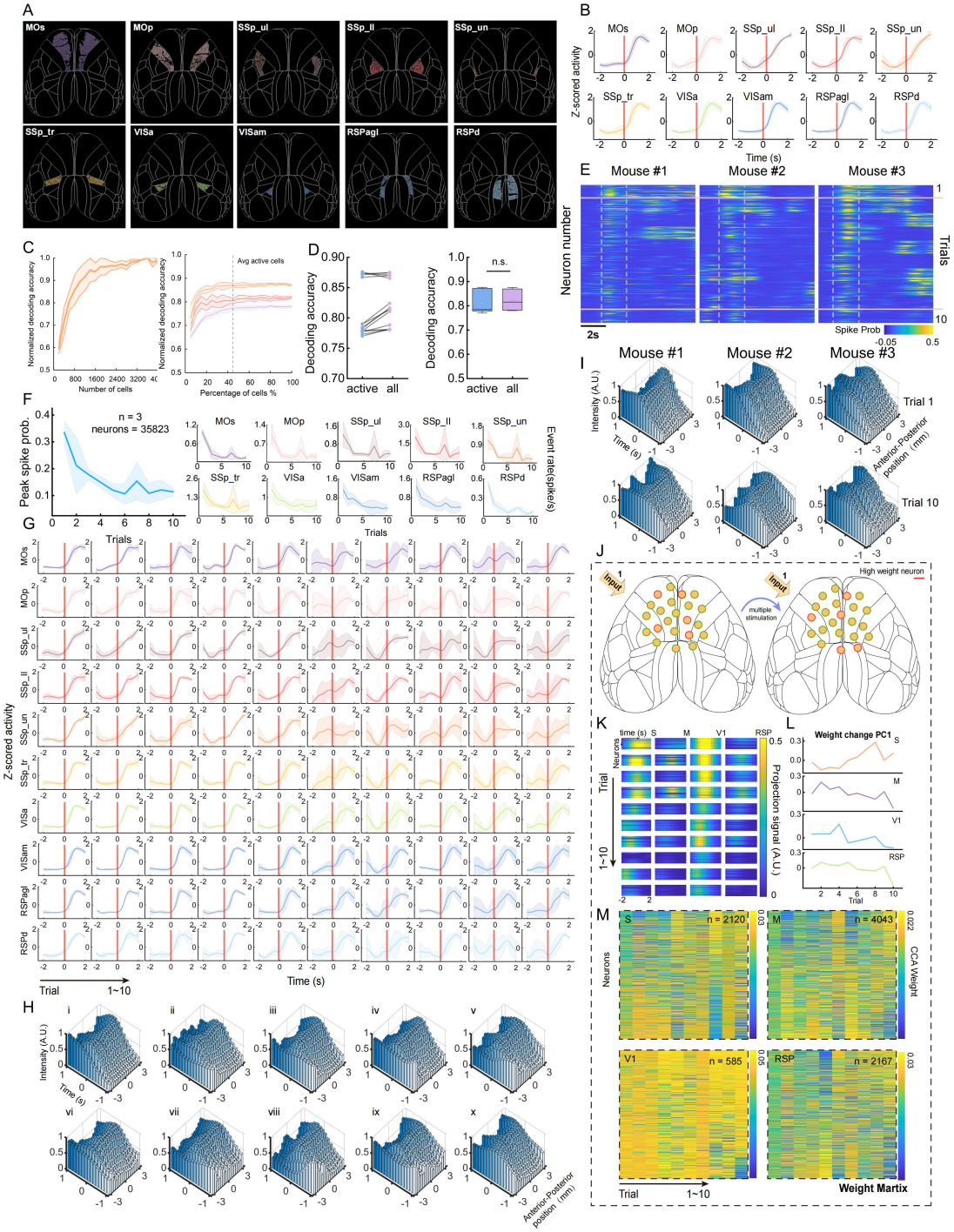

(A) Decoding performance as a function of neuronal population size. Left, performance versus absolute number of neurons. Right, performance versus the percentage of extracted neurons. Data are shown for three mice. The dashed line indicates the mean proportion of active neurons across mice, mean ± SD. **(B)** Comparisons of decoding accuracy using active neurons versus all neurons (n = 3 mice), 5 trials per mouse. **(C)** Calcium signal heatmaps across ten trials for three mice. Gray dashed lines demarcate the 4 s peri-stimulus period. Pink solid lines separate signals from

the first and last trials. The heatmaps reveal concurrent changes in response intensity and neuronal loading weights across trials. **(D)** Cortical distribution of segmented stimulus-responsive neurons. Colors denote corresponding brain regions. **(E)** Normalized neuronal spike probabilities over time and position for trials 1 and 10. Bar plots show the normalized spike probability at each time point and anterior-posterior bin for the first (Trial 1) and last (Trial 10) trials. Small neuronal populations in the posterior cortical areas of all three mice exhibited a significant temporal shift in peak activity in Trial 10 compared to Trial 1. **(F)** Left, trial-by-trial changes of peak spiking probability across 10 trials in three mice. Right, changes in calcium event rate (mean ± SD) within a 2-s window surrounding stimulus onset for individual recorded brain regions. **(G)** Average neural activity Z-scores across 10 trials for each brain region. Stimulus onset is indicated by the red vertical line. **(H)** Bar plots of normalized spike probability across 10 trials, averaged across three mice. **(I)** Trial-dependent dynamics of regional brain activity. Individual panels display neural activity Z-scores per brain region in single trials. Stimulus onset is marked by red vertical lines. **(J)** Schematic of structural reorganization in neural networks. Illustrates trial-dependent changes in single-neuron loading weights despite identical sensory inputs. **(K)** The projected activity of each area in the CCA dimensions identified across 10 trials. Population activity in S1 and V1 cortices exhibits dominant contributions to the stimulus-evoked cofluctuation mode, with trial-dependent modulation in response magnitude and phase shifts. **(L)** PC1 derived from PCA of neuronal loading weight matrices. **(M)** Heatmap of neuronal loading weights across trials. Depicts trial-dependent reorganization of loading weights within the network. **(K-M)** Representative data from one mouse.

Extended Data Fig. 6 Schematic representation and assessment of intra- and interlaminar signaling dynamics during anesthesia induction using Meso2P microscopy, related to Figure 5 and Methods.

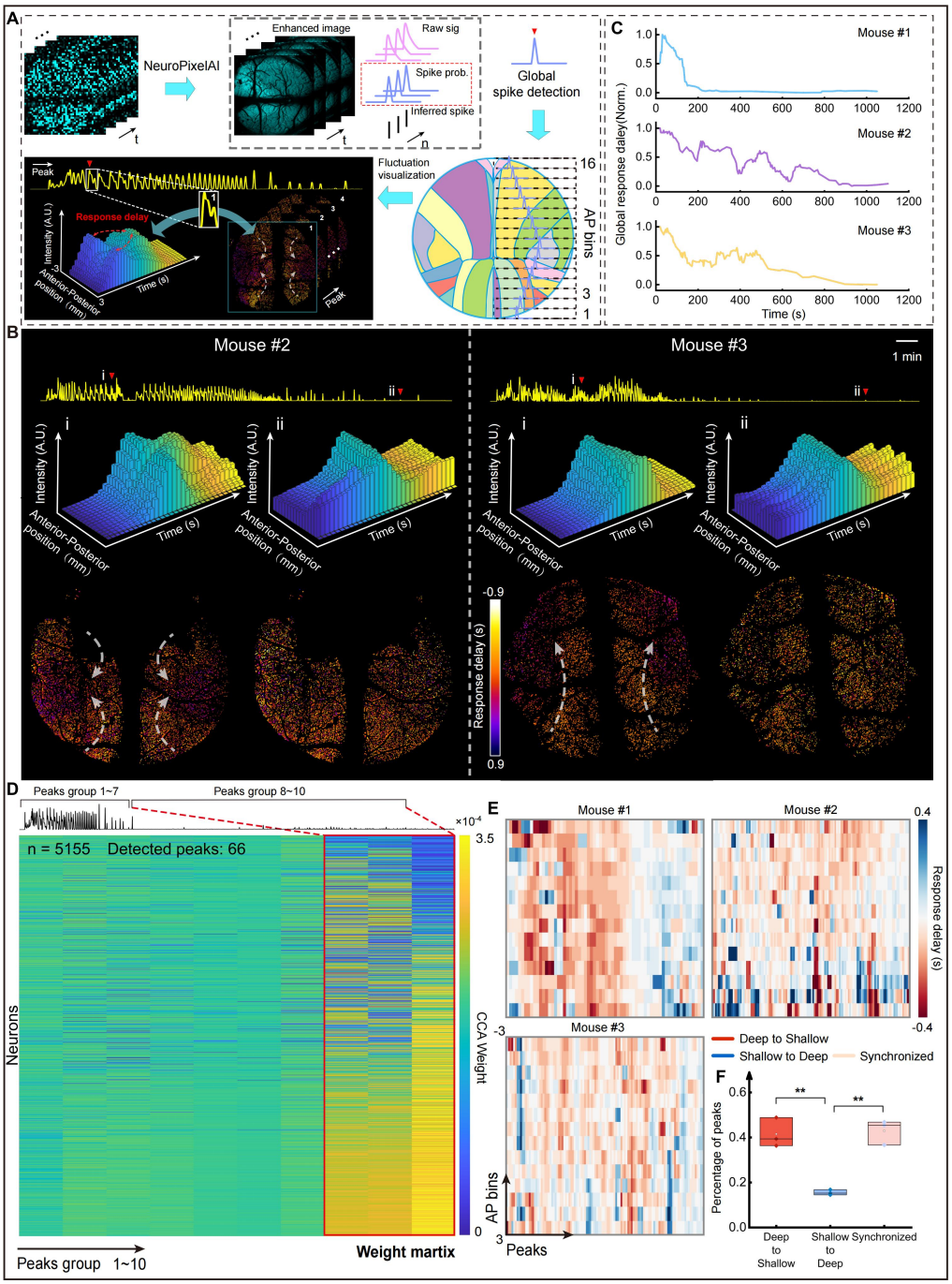

(A) Data processing pipeline for anesthetized imaging experiments. Raw image data were processed by NeuroPixelAI to extract single-neuron spike probabilities. Global spike probability traces underwent peak detection to identify multiple "synchronous" event timings. For each synchronized event, fluctuation delays were quantified at both individual anterior-posterior (AP) bins and single-neuron levels, followed by spatiotemporal visualization. **(B)** Normalized global response delays per mouse. Standard deviation (SD) of peak times in spike probabilities across 16 anterior-posterior (AP) bins was computed during anesthesia progression. This reveals a gradual

transition from spatially propagating delays (indicating asynchronous activity) to uniform synchrony across cortical regions within individual synchronous events. **(C)** Schematics of synchronized signal propagation direction in two additional mice. **(D)** Heatmap of neuronal CCA loading weights across synchronous events in an example mouse. Synchronous events were divided into 10 consecutive time bins. For each bin, cross-bin CCA identified stable activity modes during anesthesia induction. Late-phase bins exhibited significant reorganization of loading weights, concomitant with gradual uniform synchronization of cortical activity. **(E)** Heatmap of synchronized signal propagation direction between deep and shallow cortical layers during anesthesia induction. This indicates the predominant direction of signal flow during each synchronous event within individual AP bins. Red, Deep-to-shallow propagation; Blue, Shallow-to-deep propagation. **(F)** Boxplot of signal propagation direction proportions between deep and shallow cortical layers during anesthesia induction (n = 3 mice), $^{**}p < 0.01$, Tukey test.

Extended Data Fig. 7 Supplementary data for in vivo MNP imaging.

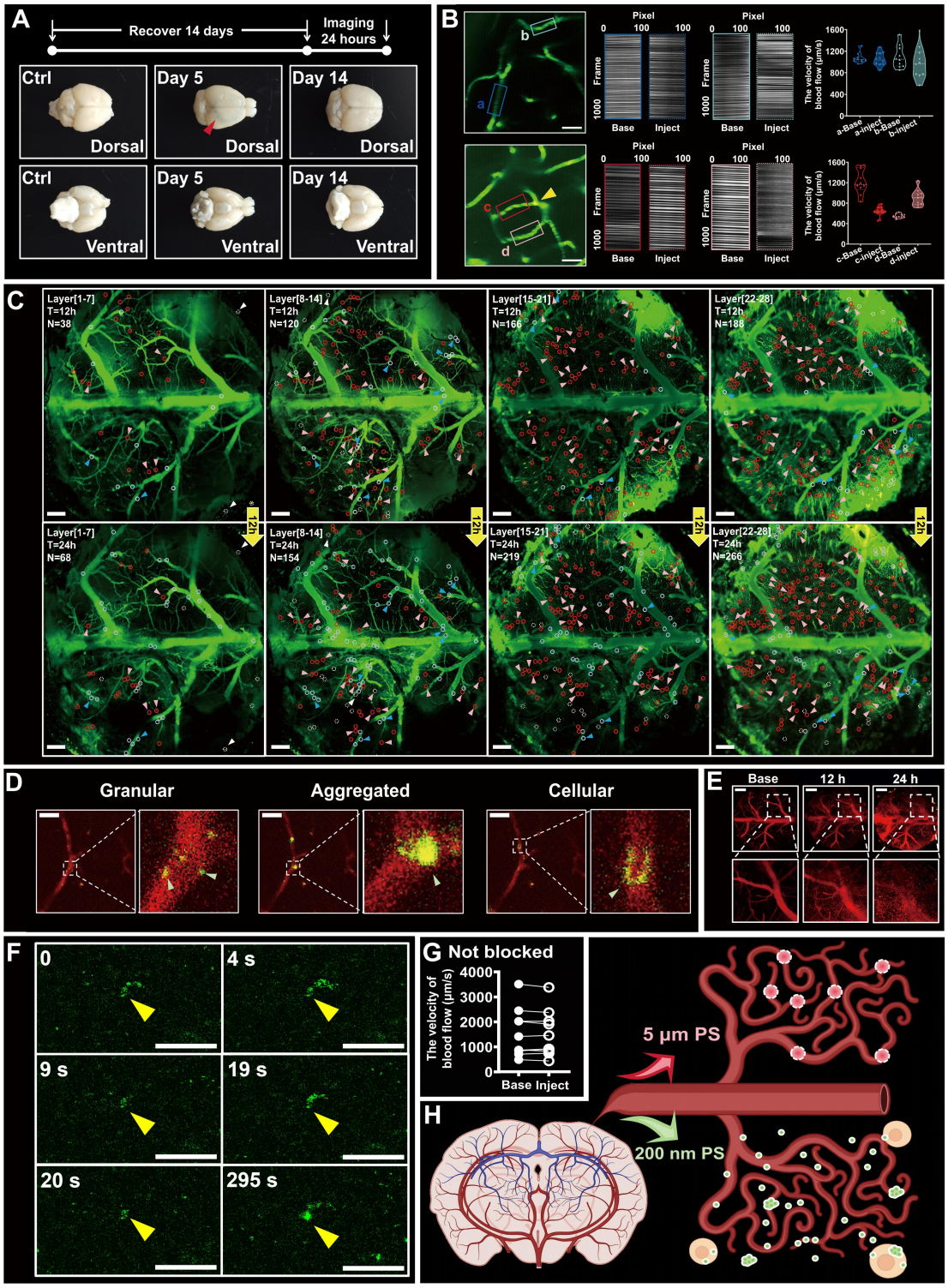

(A) Blood-brain barrier (BBB) integrity assay to determine optimal MNP imaging window; compromised BBB (red arrows). **(B)** Comparison of blood flow velocity before and 12–24 h after MP injection: vessels (green), MPs (yellow), unoccluded vessels (a, b), occluded vessel (c), adjacent vessel (d). **(C)** Cumulative distribution of MPs across vascular layers 12 h post-injection: vessels (green), MPs (red), co-localization (yellow). MPs occluding vessels < 30 μm (red circles), > 30 μm (blue circles), extravascular MPs (white dashed circles), unresolved MPs in

vessels < 30 μm (pink arrows) and > 30 μm (blue arrows). **(D)** Structural morphology of NPs in blood vessels: vessels (red), NPs (green), co-localization (yellow). **(E)** Time-dependent accumulation of NP-laden cells in the uppermost cortical layer following NP injection: vessels (red). **(F)** NP aggregation and clearance dynamics in blood vessels: NPs (green), aggregation foci (yellow arrows). **(G)** Comparison of blood flow velocity in vessels treated with NPs. **(H)** Schematic illustration of differential brain distribution patterns between 5-μm MPs and 200-nm NPs. *Scale bars*: 500 μm (C, E); 100 μm (D, F). ***See also*** **Supplementary Videos S5–9.**

Supplementary Tables

Platform	FOV×NA	FOV×NA/D	Frame resolution (pixels)	Pixel rate (Mpixel/s)	Volume Imaging	Two-photon optical stimulation
Meso2P	31.32	0.85	4096×4096	64.26	YES	YES
ULTRA[18]	32.00	0.38	4400×4800	17.53	NO	NO
Light beads[25]	19.44	0.22	1080×1200	2.85	YES	NO
2p-RAM[23]	23.76	0.26	3667×4154	10.66	NO	NO
Ultra-large FOV 2p[14]	22.40	0.62	2000×500	0.32	NO	NO
DEEP scope[21]	6.05	0.09	1024×1024	6.04	YES	NO
FASHIO-2p[15]	7.20	0.09	2048×2048	31.46	NO	NO
Quadroscope[16]	1.17	0.03	1126×600	20.27	NO	NO
Diesel2p[20]	8.10	0.09	2048×4096	32.21	NO	NO
Trepan 2p[13]	5.27	0.10	2048×2048	0.34	NO	NO

Supplementary Table 1: Comparative benchmarking of Meso2P against existing large-FOV two-photon platforms for single plane imaging.

1532

Platform	Volume size (mm)	Volume resolution (voxels)	Volume rate (Hz)	Simultaneous imaging plane	Voxel rate (Mpixel/s)
Meso2P	6×6×0.5	2048×2048×28	1	28	117.44
Light beads[25]	5.4×6×0.5	1080×1200×30	2.2	30	85.54
DEEP scope[21]	3.23×3.23×0.08	1030×515×5	2.2	5	5.83

1533 **Supplementary Table 2: Comparative benchmarking of Meso2P against existing**

1534 **large-FOV two-photon platforms for volume imaging.**

1535

Platform	FOV (mm^2)	NA	Objective diameter (mm)	Frame rate (Hz)
Meso2P	36	0.87	37	3.83
ULTRA[18]	64	0.5	85	0.83
Light beads[25]	32.4	0.6	90	2.2
2p-RAM[23]	23.76	1	90	0.7
Ultra-large FOV 2p[14]	80	0.28	36	0.32
DEEP scope[21]	10.4329	0.58	67	5.76
FASHIO-2p[15]	9	0.8	84	7.5
Quadroscope[16]	2.25	0.52	38.21	30
Diesel2p[20]	15	0.54	90	3.84
Trepan 2p[13]	12.25	0.43	50.8	0.08

1536 **Supplementary Table 3: Specific parameter values of comparison benchmark**
1537 **between Meso2P and existing large FOV two-photon platforms.**

Supplementary Notes

Supplementary Notes 1: Quantitative benchmarking of Meso2P against large-FOV two-photon microscopes

We first compared single-plane imaging performance of Meso2P with state-of-the-art mesoscale 2P systems (Supplementary Tables 1 and 2). Using the conventional figure-of-merit FOV × NA, Meso2P exceeds all existing platforms and matches the ULTRA microscope, yet it does so with a standard 4× objective. When normalised by objective diameter (FOV × NA / D), Meso2P leads the field by a substantial margin.

In throughput, Meso2P delivers a pixel rate twice that of the next fastest system. It can operate at 4,096 × 4,096 pixels per frame (3.83 Hz), providing the combination of resolution and speed required for large-scale calcium imaging.

Among currently available mesoscopes, Meso2P is one of the few that can be upgraded to volumetric operation. Its voxel rate outperforms all reported volumetric scanners (Supplementary Table 3), and it is the only platform that maintains single-plane spatial resolution and frame rate while simultaneously acquiring 2–4 planes.

Finally, Meso2P is one of the rare large-FOV instruments that integrates two-photon optogenetic stimulation without compromising imaging performance, enabling tightly co-registered perturbation and read-out within the same optical core.